ACS APPLIED MATERIALS & INTERFACES

Research Article

www.acsami.org

Facile Synthesis of Novel Redox-Mediator-free Direct Z-Scheme $CaIn_2S_4$ Marigold-Flower-like/TiO_2 Photocatalysts with Superior Photocatalytic Efficiency

Wan-Kuen Jo and Thillai Sivakumar Natarajan*

Department of Environmental Engineering, Kyungpook National University, 80 Daehakro, Bukgu, Daegu 702-701, Republic of Korea

Supporting Information

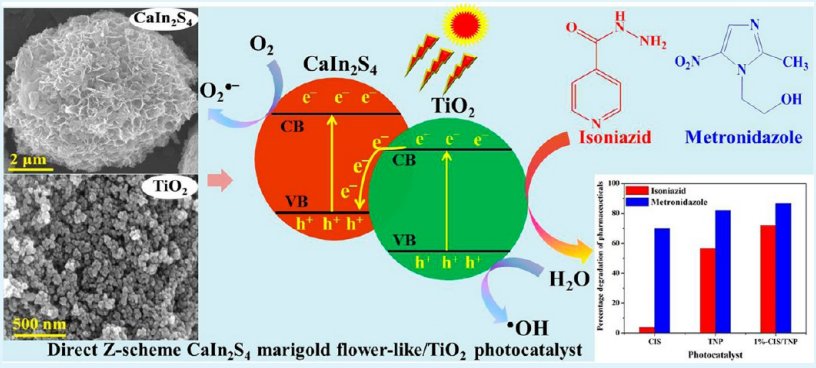

ABSTRACT: Novel redox-mediator-free direct Z-scheme $CaIn_2S_4$ marigold-flower-like/TiO_2 (CIS/TNP) photocatalysts with different $CaIn_2S_4$ weight percentages were synthesized using a facile wet-impregnation method. Uniform hierarchical marigold-flower-like $CaIn_2S_4$ (CIS) microspheres were synthesized using a hydrothermal method. Field-emission scanning electron microscopy and transmission electron microscopy analyses suggested that the formation and aggregation of nanoparticles, followed by the growth of petals or sheets and their subsequent self-assembly, led to the formation of the uniform hierarchical marigold-flower-like CIS structures. The photocatalytic degradation efficiency of the direct Z-scheme CIS/TNP photocatalysts was evaluated through the degradation of the pharmaceutical compounds isoniazid (ISN) and metronidazole (MTZ). The direct Z-scheme $CaIn_2S_4$ marigold-flower-like/TiO_2 (1%-CIS/TNP) photocatalyst showed enhanced performance in the ISN (71.9%) and MTZ (86.5%) photocatalytic degradations as compared to composites with different $CaIn_2S_4$ contents or the individual TiO_2 and $CaIn_2S_4$. A possible enhancement mechanism based on the Z-scheme formed between the CIS and TNP for the improved photocatalytic efficiency was also proposed. The recombination rate of the photoinduced charge carriers was significantly suppressed for the direct Z-scheme CIS/TNP photocatalyst, which was confirmed by photoluminescence analysis. Radical-trapping studies revealed that photogenerated holes (h^+), $^{\bullet}OH$, and $O_2^{\bullet-}$ are the primary active species, and suggested that the enhanced photocatalytic efficiency of the 1%-CIS/TNP follows the Z-scheme mechanism for transferring the charge carriers. It was further confirmed by hydroxyl ($^{\bullet}OH$) radical determination via fluorescence techniques revealed that higher concentration of $^{\bullet}OH$ radical were formed over 1%-CIS/TNP than over bare CIS and TNP. The separation of the charge carriers was further confirmed using photocurrent and electron spin resonance measurements. Kinetic and chemical oxygen demand analyses were performed to confirm the ISN and MTZ degradation. The results demonstrated that the direct Z-scheme CIS/TNP photocatalyst shows superior decomposition efficiency for the degradation of these pharmaceuticals under the given reaction conditions.

KEYWORDS: *TiO_2, $CaIn_2S_4$ marigold-flower-like, hierarchical, self-assembly, redox-mediator-free, Z-scheme, isoniazid, metronidazole*

INTRODUCTION

Since their discovery, heterogeneous TiO_2-photocatalyst-based processes have been efficiently applied for environmental remediation and energy production.[1−9] However, the commercialization of these processes has been limited due to the high recombination rate of the photogenerated electron−hole pairs and the very poor visible-light response by TiO_2 due to its high band gap (3.2 eV). To increase the lifetimes of charge carriers and the visible-light photocatalytic performance of TiO_2, different modifications have been attempted; however, the problems remain unresolved.[10−18] As alternatives, metal-sulfide-based visible-light photocatalysts have been employed. However, in addition to their toxicity, these materials are highly unstable during the photocatalytic reaction and

Received: May 6, 2015
Accepted: July 17, 2015
Published: July 17, 2015

DOI: 10.1021/acsami.5b03935
ACS Appl. Mater. Interfaces 2015, 7, 17138−17154

insufficiently efficient to meet practical requirements. To surmount these problems, ternary chalcogenide AB_2X_4 (A = Cu, Zn, Cd, Ca, etc.; B = In, Ga, Al; X = S, Se, Te)-based visible-light photocatalysts have recently drawn attention due to their unique electronic and optical properties, as well as excellent photo- and chemical stabilities.[19−22] Due to their narrow band gaps, these catalysts have been predominantly applied in H_2 production. In 2003, Lei et al. first developed the novel sphere-like $ZnIn_2S_4$.[23] Later, Kale et al.[24] synthesized nanotube and marigold structures of ternary $CdIn_2S_4$. Recently, Ding et al.[25,26] synthesized cubic and monoclinic $CaIn_2S_4$ for H_2 production. However, for an isolated AB_2X_4 component, it is very challenging to migrate the photogenerated electron−hole pairs and suppress their rate of recombination. Consequently, the coupling of AB_2X_4 materials with other semiconductors, metals (metal loading), or reduced graphene oxide (RGO) has been studied to enhance the lifetimes of the charge carriers.[27−30] However, the efficiencies of the systems must be improved to meet large-scale commercial requirements. Because transition-metal-based systems are expensive and ecologically unfriendly, it has become imperative to explore the alternative, inexpensive, metal-based ternary metal sulfides for enhanced photocatalytic efficiency. For example, although $CaIn_2S_4$ is the cheapest alkali earth metal based system, no detailed investigations have focused on its synthesis, morphology, or coupling with other semiconductors for possible improvements in photocatalytic decomposition efficiency.

It is well-known that the construction of heterojunction or direct Z-scheme photocatalysts by the coupling of one semiconductor with another is a relatively effective method for promoting photocatalytic performance by the efficient separation of charge carriers. Along these lines, the development of redox-mediator-free direct Z-scheme photocatalysts has aroused significant scientific interest. Recently, Yang et al.[31] synthesized TiO_2- and CuO-coupled $ZnIn_2S_4$ heterojunction photocatalysts which efficiently suppressed recombination rates and exhibited enhanced photocatalytic efficiency. However, the design of direct Z-scheme photocatalysts by the coupling of AB_2X_4 materials with other metal oxide semiconductors has been limited. The coupling of $CaIn_2S_4$ with other semiconductors, in particular, has not been explored. We expected that the coupling of TiO_2 with $CaIn_2S_4$ would form a direct Z-scheme photocatalyst because of its suitable valence band (VB) and conduction band (CB) edge positions, which could suppress the recombination rate and enhance the visible-light response of TiO_2. Thus, the electrons and holes in the highly negative and positive potentials of the CB and VB edges of $CaIn_2S_4$ (−1.1 eV) and TiO_2 (+2.91 eV) could produce a greater number of superoxide ($O_2^{\bullet-}$) and hydroxyl ($^{\bullet}OH$) radicals and impart increased photocatalytic decomposition efficiency.

The antibiotics isoniazid (ISN) and metronidazole (MTZ) are used for the treatment of tuberculosis and the infectious diseases caused by anaerobic bacteria and protozoa, respectively. Both are highly soluble in water and nonbiodegradable, and thus, their elimination from effluent streams has received considerable attention as they are highly toxic and carcinogenic. To date, TiO_2, CdS, ZnS, Zn_2GeO_4, $ZnSnO_3$, ZnO/RGO, $BiVO_4$, $BiVO_4/FeVO_4$, and $CdS/g\text{-}C_3N_4$, photocatalysts have been used for the decomposition of MTZ,[32−38] whereas only a single study has investigated ISN degradation using TiO_2 and ZnO photocatalysts.[39] No detailed study has been performed on the degradation of these pharmaceuticals using a direct Z-scheme photocatalytic system.

Here, we report the synthesis of hierarchical marigold-flower-like $CaIn_2S_4$ ternary metal sulfides using a hydrothermal method; subsequently, the novel direct Z-scheme $CaIn_2S_4$ marigold-flower-like/TiO_2 photocatalysts were successfully synthesized using a facile wet-impregnation method. The growth mechanism for formation of hierarchical marigold-flower-like $CaIn_2S_4$ was proposed. The prepared photocatalysts were utilized for the degradation of ISN and MTZ and compared against the activities of the pure TiO_2 and marigold-flower-like $CaIn_2S_4$ photocatalysts. The new direct Z-scheme $CaIn_2S_4$ marigold-flower-like/TiO_2 photocatalysts displayed enhanced photocatalytic efficiency over the individual $CaIn_2S_4$ and TiO_2 catalysts for the degradation of ISN and MTZ under our reaction conditions. A degradation mechanism for the improved photocatalytic performance was also proposed.

EXPERIMENTAL SECTION

Photocatalysts Synthesis. Calcium indium sulfide ($CaIn_2S_4$) was synthesized by the hydrothermal method.[30] Briefly, calcium nitrate tetrahydrate (5 mmol), indium nitrate hydrate (10 mmol), and thioacetamide (40 mmol) were dissolved in ultrapure water (80 mL) and stirred for 30 min at room temperature. Then, the reaction mixture was transferred into a 100 mL Teflon-lined stainless steel autoclave and heated at 393 K for 24 h. Thereafter, the autoclave was cooled naturally to ambient temperature. The orange precipitate was centrifuged and repeatedly washed with copious amounts of ultrapure water and absolute ethanol. The final material, labeled as CIS, was dried at 343 K for 12 h.

Composites of titanium dioxide nanoparticles (TNPs) loaded with different weight percentages of CIS (denoted as x%-CIS/TNP; x = 1, 3, 5, 7, and 10) were synthesized using a simple wet impregnation method. First, a TiO_2 suspension was prepared by dispersing the NPs in methanol (50 mL) via ultrasonication for 30 min. Then, the calculated amount of CIS was added into the suspension to afford the desired weight percentage of CIS. The mixture was stirred at room temperature for 24 h in the fume hood. Afterward the obtained solid materials were dried at 348 K for 12 h. Subsequently, the materials were ground using a mortar and pestle.

Photocatalytic Activity. The photocatalytic activities of the CIS, TNP, and direct Z-scheme x%-CIS/TNP (x = 1, 3, 5, 7, and 10) photocatalysts were studied by monitoring the degradation behaviors of aqueous solutions of ISN and MTZ using a quartz immersion-well-type photocatalytic reactor.[6] In the photocatalytic degradation reaction, a suspension containing the photocatalyst (100 mg) and an aqueous solution of either ISN or MTZ (500 mL, 50 mg/L) was loaded in the outer borosilicate glass container, ultrasonicated for 2 min, and then stirred in the dark for 30 min to establish an adsorption−desorption equilibrium between the photocatalyst and the substrates. Subsequently, the suspension was irradiated under a 200 W mercury vapor lamp. The mixture was continuously stirred throughout the reaction, and to prevent any effects on the degradation efficiency by inadvertent heating from the lamp, the temperature was controlled by circulating the water throughout the experiment. From the irradiated suspension, aliquots (7 mL) were withdrawn by syringe at 10 min intervals for the first 1 h and then every 1 h up to 4 h for absorbance measurements by UV spectroscopy. Before UV analysis, each aliquot was centrifuged to separate the photocatalyst (10 000 rpm, 30 min), and then the absorbance was determined using a UV−visible spectrophotometer (Shimadzu, UV-2600). The concentrations of ISN and MTZ in the degraded solutions were obtained from their respective calibration curves (concentration vs absorbance) prepared with different known concentrations; then, the percentage degradation was calculated. A blank reaction (without photocatalyst) was performed in the presence of light irradiation only, for comparison with the effects of the photocatalysts on degradation. Cyclic degradation experiments were performed to evaluate the reusability

DOI: 10.1021/acsami.5b03935
ACS Appl. Mater. Interfaces 2015, 7, 17138−17154

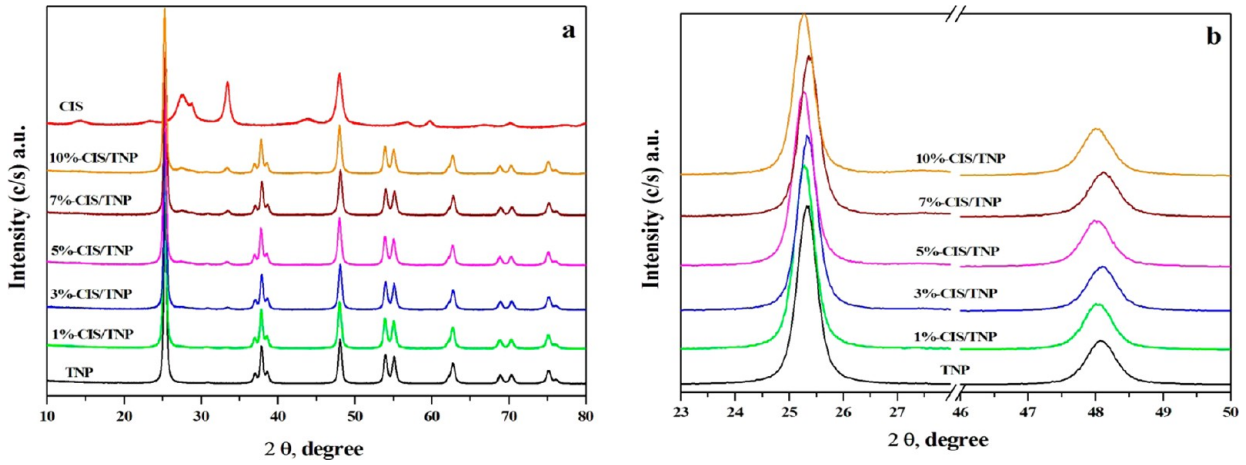

Figure 1. PXRD patterns of (a) CIS, TNP, and *x*%-CIS/TNP composites, and (b) expanded anatase peaks of TiO_2 at 25.32 and 48.08°.

Table 1. Surface Areas, Pore Volumes, Mean Pore Diameters, and Band Gaps of the Synthesized Photocatalytic Materials

	phase percentage						
photocatalyst	anatase	brookite	surface area (m^2/g)	pore volume (cm^3/g)	mean pore diameter (nm)	band edge (nm)	band gap (eV)
TNP	98.3	1.7	56.74	0.302	21.27	388	3.20
CIS			93.52	0.081	3.47	626	1.98
1%-CIS/TNP	98.2	1.8	57.21	0.123	8.63	389	3.18
3%-CIS/TNP	98.1	1.9	58.83	0.122	8.30	392	3.16
5%-CIS/TNP	97.9	2.1	58.45	0.311	21.26	393	3.15
7%-CIS/TNP	97.6	2.4	60.27	0.309	20.54	394	3.14
10%-CIS/TNP	97.8	2.2	65.52	0.326	19.91	396	3.12

of the photocatalyst. After each cycle of experiment, the photocatalyst was separated by centrifugation, dried and used for the next cycle of degradation experiment without any pretreatment.

Further confirmation of ISN and MTZ degradation was performed by chemical oxygen demand (COD) analysis of the degraded samples using a HACH DR/4000U spectrophotometer. A sample (2 mL) was added to the COD reagent and digested for 2 h at 423 K in a HACH Digital Reactor Block (DRB200). Afterward, the mixture was cooled to ambient temperature, and the COD was analyzed.

Detection of Reactive Species. It is well-known that in photocatalytic degradation reactions, hydroxyl ($^{\bullet}OH$) radicals, electron (e^-), holes (h^+), and superoxide ($O_2^{\bullet-}$) radical anions are the major active species in the oxidation and reduction of target pollutants. To determine the reactive radical species involved in the degradation of ISN and MTZ, trapping experiments were performed by introducing various scavengers such as isopropyl alcohol (IPA, 10 mmol/L), ammonium oxalate (AO, 6 mmol/L), and 1,4-benzoquinone (BQ, 0.1 mmol/L) into the reaction to scavenge the $^{\bullet}OH$, h^+, and $O_2^{\bullet-}$ species. The trapping experiment procedures were similar to that of the degradation experiment, with the various scavengers introduced separately into the aqueous substrate solution before addition of the photocatalyst.

Analysis of Hydroxyl ($^{\bullet}OH$) Radical Formation. The superior photocatalytic efficiency of 1%-CIS/TNP photocatalyst was confirmed by determination of hydroxyl ($^{\bullet}OH$) radical formation during the course of the reaction. The hydroxyl ($^{\bullet}OH$) radical formation on the surface of CIS, TNP, and 1%-CIS/TNP photocatalysts under light irradiation was determined by a fluorescence technique with terephthalic acid (TA) as a probe molecule. TA reacts with $^{\bullet}OH$ radical formed in the reaction to produce a highly fluorescent product, 2-hydroxyterephthalic acid. The intensity of 2-hydroxyterephthalic acid peak corresponds to the amount of $^{\bullet}OH$ radicals formed during the reaction.[40] The experimental procedure was similar to that of photocatalytic degradation except that pollutants solution was replaced by terephthalic acid (5×10^{-4} M) in dilute NaOH solution (2×10^{-3} M). Then, the reaction mixture was subjected to light irradiation, sampling was performed and separated the photocatalyst by centrifugation. Subsequently, the formed 2-hydroxyterephthalic acid product (λ = ~ 425–432 nm) was analyzed by spectrofluorophotometer (Shimadzu, RF-5301PC) with the excitation wavelength of 315 nm.

RESULTS AND DISCUSSION

PXRD Analysis. The PXRD pattern of CIS displays diffraction peaks at 2θ = 14.58, 23.38, 27.48, 28.82, 33.42, 43.94, 48.02, 56.96, 59.7, 66.94, and 70.16°, indexed to the (111), (220), (311), (222), (400), (511), (440), (533), (622), (731), and (800) planes of cubic CIS (Figure 1a).[25,26,30] Peaks corresponding to binary sulfides, oxides, and unreacted reactants were not observed, indicating the purity of the synthesized cubic CIS. For the TNP and *x*%-CIS/TNP composites, the peaks at 2θ = 25.32, 37.04, 37.82, 38.62, 48.08, 53.96, 55.10, 62.16, 68.86, 70.28, 75.12, and 76.08° correspond to the diffractions of the (101), (103), (004), (112), (200), (105), (211), (213), (116), (220), (301), and (215) crystal planes of the anatase phase of TiO_2 (JCPDS-00-021-1272). In addition, a less intense diffraction peak, observed at 2θ = 30.83° is attributed to the (121) crystal plane of the brookite phase of TiO_2 (JCPDS-00-029-1360). The anatase and brookite phase percentages were calculated using eqs S2–S4. The results, shown in Table 1, reveal that the TNPs comprise 98% anatase and 2% brookite, whereas in the composite materials, slight decreases and increases in the anatase and brookite phase percentages were observed, respectively. This may be due to the presence of the CIS in the composite materials. The calculated crystallite sizes of the anatase peaks of TiO_2 were 38.40 (TNP), 38.60 (1%-CIS/TNP), 39.26 (3%-CIS/TNP), 38.69 (5%-CIS/TNP), 38.88 (7%-CIS/TNP), and 38.88 nm (10%-CIS/TNP), indicating

DOI: 10.1021/acsami.5b03935
ACS Appl. Mater. Interfaces 2015, 7, 17138–17154

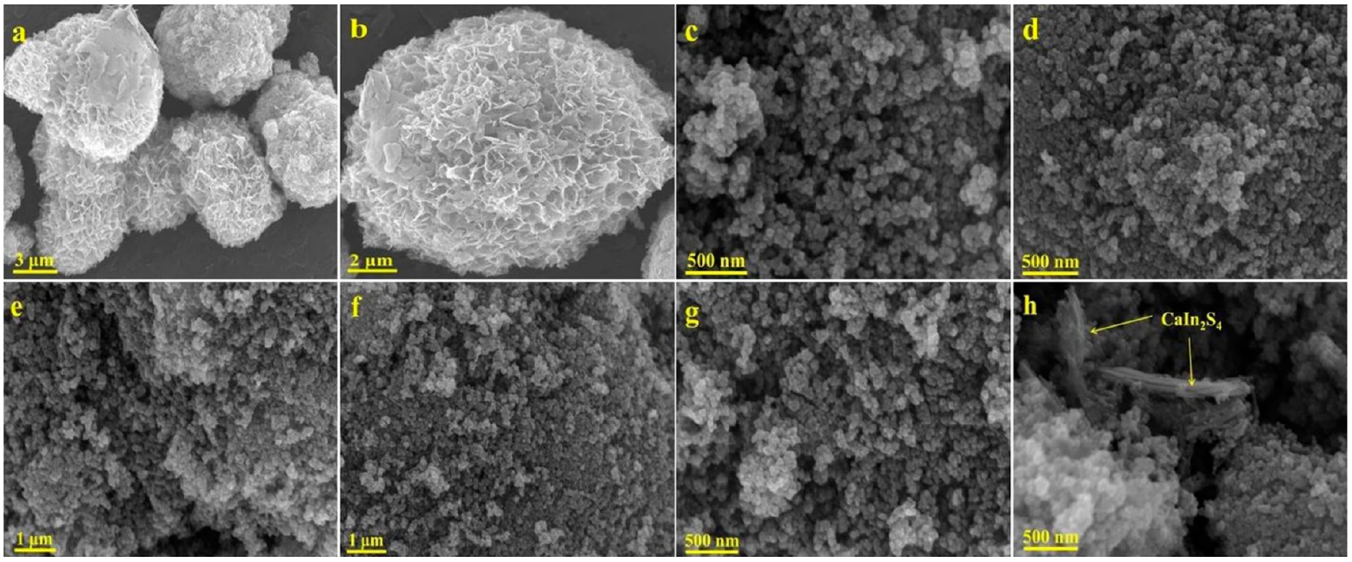

Figure 2. FE-SEM images of (a and b) CIS, (c) TNP, (d) 1%-CIS/TNP, (e) 3%-CIS/TNP, (f) 5%-CIS/TNP, (g) 7%-CIS/TNP, and (h) 10%-CIS/TNP composites.

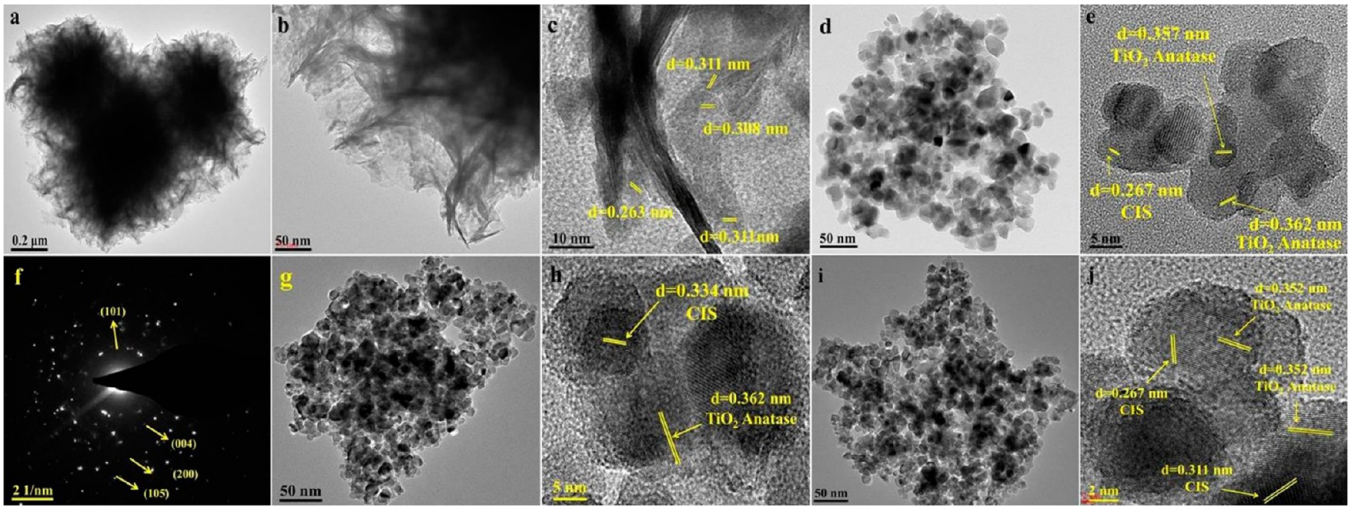

Figure 3. TEM images of (a and b) CIS, (c) HR-TEM image of b, (d) TNP, (e) 1%-CIS/TNP, (f) SAED pattern of e, (g) 5%-CIS/TNP, (h) HR-TEM image of g, (i) 10%-CIS/TNP, and (j) HR-TEM image of i.

that the addition of CIS did not exert any significant influence on the crystallite size. Moreover, the intensities of the diffraction peaks corresponding to CIS at 27.48 and 33.42° in the composite materials increased with the rising CIS content (Figure 1a). These results indicate the coexistence of the CIS and TiO_2 in the synthesized composites. For the anatase peaks at 25.32 and 48.08°, the intensities decreased and the positions shifted to lower diffraction angles with the increments in CIS loading (Figure 1b). The decreases in the intensities and the shifts of the peaks toward lower diffraction angles clearly confirm the successful synthesis of the redox-mediator-free direct Z-scheme CIS/TNP composite materials.

Field-Emission Scanning Electron Microscopy (FE-SEM) Analysis. The FE-SEM image of CIS (Figure 2a) reveals that it consists of monodispersed uniform microspheres with marigold-flower-like morphologies. A magnified FE-SEM image (Figure 2b) shows that the microspheres are composed of numerous, very thin, densely packed "petals", which leads to the marigold-flower-like morphology. Similar morphologies have been reported by Shen et al.[41] and Chen et al.[42] in the synthesis of $ZnIn_2S_4$. However, previous reports for CIS have described a mixture of nanoparticles and nanosheet-like morphologies.[25,26,30] Figure 2c shows the spherical morphology of TiO_2, which was unchanged upon the addition of CIS (Figure 2d–h), although some TiO_2 agglomeration did occur. In the 1–7%-CIS/TNP composites, the marigold-flower-like microspherical morphology of the CIS is not observed (Figure 2d–g), although it is clearly visible in the 10%-CIS/TNP composite (Figure 2h, marked with yellow arrow). However, the CIS loading is evident from the change in the TiO_2 color from white to orange (Figure 7). In the 10%-CIS/TNP composite (Figure 2h), the added CIS appears to exhibit a curved sheet- or tube-like structure. It is possible that, while stirring during preparation, some of the thin petals of the microspheres were exfoliated and formed curled sheets, which were subsequently rolled into tube-like structures. Similar results have been reported by Gou et al.[22] in the $ZnIn_2S_4$ system. The failure to observe the CIS in the 1–7%-CIS/TNP

DOI: 10.1021/acsami.5b03935
ACS Appl. Mater. Interfaces 2015, 7, 17138–17154

composites may be due to its uniform distribution; however, the FE-SEM-EDX analysis of the 10%-CIS/TNP composite (Figure S2) confirmed the presence of Ti, O, Ca, In, and S. The marigold-flower-like microspherical morphologies of the CIS and its composites were further confirmed by TEM analysis.

Transmission Electron Microscopy (TEM) Analysis. The TEM image of CIS (Figure 3a) clearly shows that its marigold-flower-like microspherical morphology is derived from a large number of sheets, which is inaccordance with the FE-SEM results. The TEM image further reveals that the sheets are very thin and interwoven, forming the marigold-flower-like morphology (Figure 3b). The high-resolution transmission electron microscopy (HR-TEM) image of the thin sheets (Figure 3c) demonstrates the lattice lines of the marigold-flower-like CIS with intervals of 0.311 and 0.308 and 0.263 nm, corresponding to the (222) and (400) crystal planes of cubic CIS. In addition to the marigold-flower-like structure of CIS, CIS NPs were observed in the HR-TEM image of CIS (Figure S3a). This suggests that the formation of CIS NPs could be an initial step in the generation of the CIS marigold-flower-like nanostructures. Furthermore, the integrity of the marigold-flower-like microspherical morphology was maintained despite being subjected to ultrasonic treatment before the TEM analysis, suggesting the structural robustness of the synthesized microspheres. To our knowledge, the previous studies of synthesized $CaIn_2S_4$ have shown it to consist of a mixture of NPs, nanorods, and nanosheet-like structures.[25,26,30] However, in this case, we obtained a large number of uniform CIS microspheres with marigold-flower-like morphologies and diameters of 1.1−1.5 μm (Figure S3b). Hence, this is the first report of the synthesis of uniform marigold-flower-like CIS microspheres.

The TEM image in Figure 3d shows the spherical morphology of the TNP. The presence of the marigold-flower-like CIS was not observed in the TEM images of the 1, 5, or 10%-CIS/TNP composites, which may be due to its uniform distribution in the TNP. However, the HR-TEM image of 1%-CIS/TNP (Figure 3e) clearly shows the lattice lines of both the TNP and CIS materials. The lattice fringes distance of 0.267 nm corresponds to the (400) plane of cubic CIS, whereas the 0.357 and 0.362 nm distances may be attributed to the (101) plane of anatase TiO_2. The presence of CIS and TNP in the 1%-CIS/TNP was also confirmed by elemental mapping analysis. The high-angle annular dark field (HAADF, Figure 4a) image and element mapping analysis (Figure 4b−f) of 1%-CIS/TNP reveals the presence of Ti, O, Ca, In, and S, suggesting the coexistence of both CIS and TNP. These data also show that the CIS is uniformly distributed in the composite, affording intimate contact between the two materials. The selected area electron diffraction (SAED) pattern of the 1%-CIS/TNP composite (Figure 3f) corresponds to the TNP, substantiating its polycrystalline nature. The diffraction pattern matches with the (101), (004), (200), and (105) planes of anatase TiO_2.

From Figure 3f, it is clear that the circular diffraction patterns are not uniform, due to the presence of both CIS and TNP in the composite materials. The TEM images of the 5 and 10%-CIS/TNP (Figure 3g,i) revealed that the dark regions increased with increments in CIS loading, and thus may be related to the presence of CIS; the gray areas were denoted as TNP. These assignments were confirmed by the elemental mapping analysis of the Z-scheme 10%-CIS/TNP material (Figure S3c−h), which showed the presence of Ti, O, Ca, In, and S elements

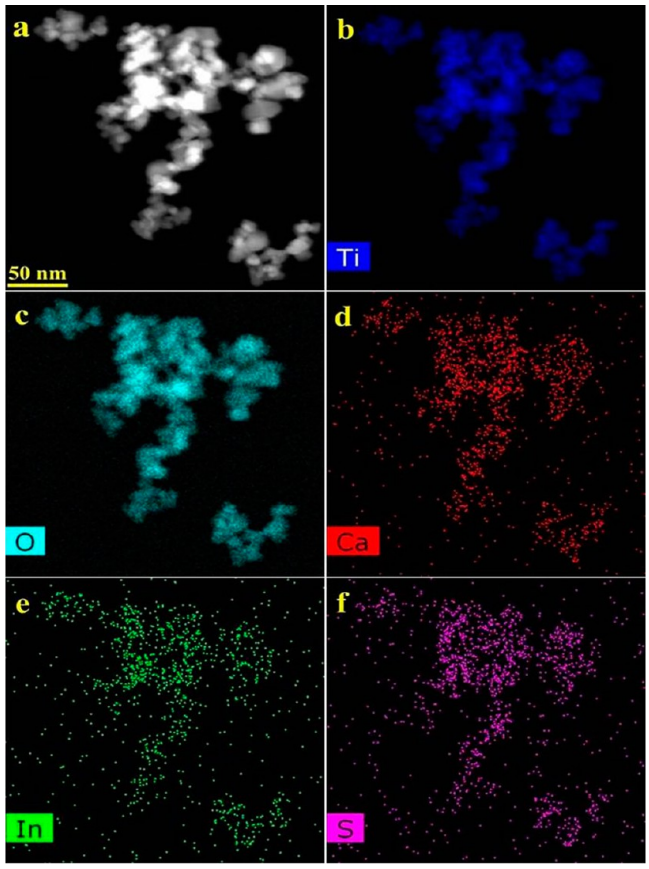

Figure 4. (a) HAADF image and elemental mapping images of (b) Ti, (c) O, (d) Ca, (e) In, and (f) S elements of the 1%-CIS/TNP composite material.

and further supported the identification of the dark and gray regions as CIS and TNP, respectively. It was apparent that the CIS is uniformly distributed throughout the TNP, confirming the construction of the Z-scheme and close contact of the two materials through the wet-impregnation method. This intimate contact is beneficial for the separation of photogenerated charge carriers in the direct Z-scheme CIS/TNP photocatalyst.

Though the marigold-flower-like morphology of CIS was not observed, the HR-TEM images of the 5 and 10%-CIS/TNP Z-scheme photocatalysts (Figure 3h,j) obviously show the lattice lines corresponding to both the CIS and TNP materials. The lattice fringe intervals of 0.334, 0.311, and 0.267 nm are indexed to the (311), (222), and (400) crystal planes of cubic CIS, whereas those at 0.352 and 0.362 nm correspond to the (101) plane of anatase TiO_2. From the FE-SEM and TEM results, we conclude that the direct Z-scheme $CaIn_2S_4$ marigold-flower-like/TiO_2 photocatalysts were successfully synthesized.

Growth Mechanism of $CaIn_2S_4$. Generally, different nanomaterial morphologies can be obtained during synthesis by the addition of various surfactants. In this instance, however, the uniform marigold-flower-like microspherical morphology of the CIS synthesized without addition of any surfactants. It is well-known that, in the absence of surfactants, the geometrical building blocks or individual building components of a material may pave the way for the formation of a marigold-flower-like morphology by a self-assembly process.[43,44] On the basis of FE-SEM and TEM images, we proposed a possible formation mechanism for the CIS microspheres with the marigold-flower-like morphology, and is schematically represented in Scheme 1.

DOI: 10.1021/acsami.5b03935
ACS Appl. Mater. Interfaces 2015, 7, 17138−17154

Scheme 1. Schematic Representation of the Formation Mechanism of Marigold Flower-Like $CaIn_2S_4$ (CIS) Structure

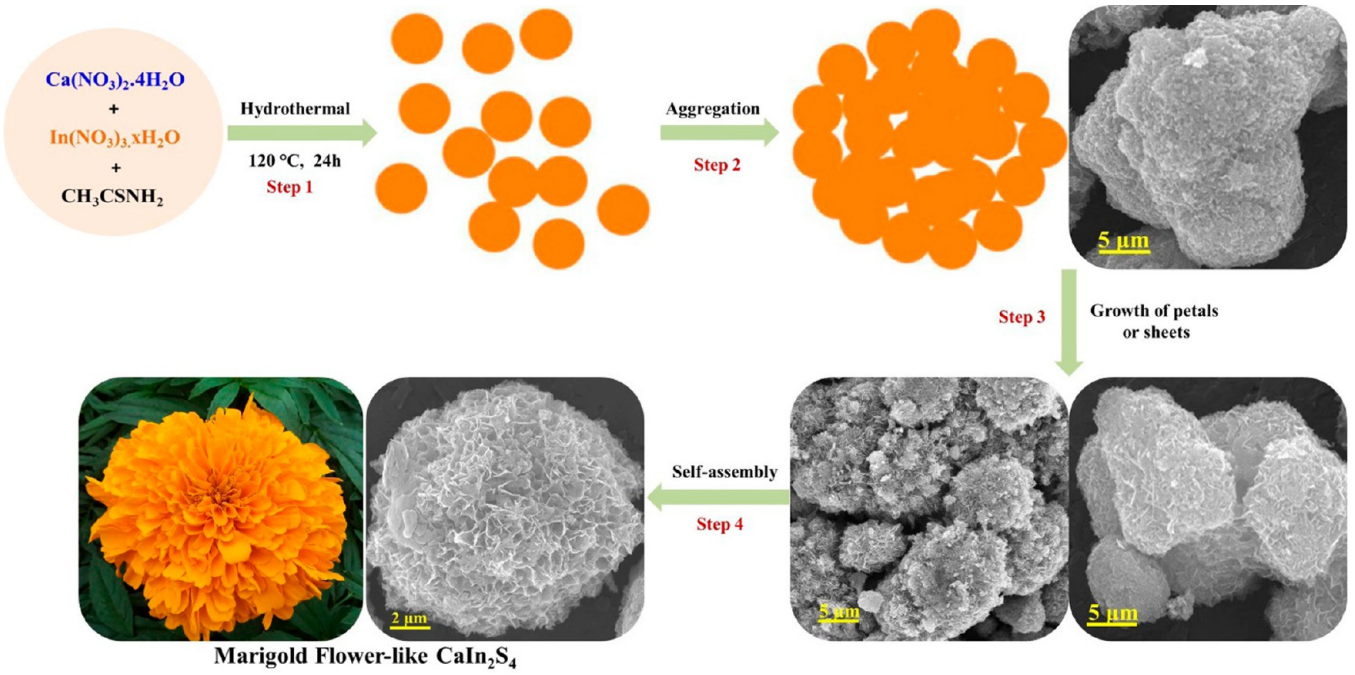

Under the reaction conditions, the nucleation of a precursor leads to the formation of the CIS NPs (step 1). Subsequently, these NPs tend to aggregate to reduce their surface energies, forming the CIS microspheres (step 2). At high temperature, the petal- or sheet-like morphology of the $CaIn_2S_4$ starts to grow from the microspheres (step 3, Figure S4a−c); single petal- or sheet-like morphologies can be clearly observed in the TEM analysis (Figure S4f). Then, the prolonged hydrothermal reaction may lead to the self-assembly of these petals or sheets (step 4) into the uniform hierarchical marigold-flower-like morphology of CIS (Figure S4d). The magnified FE-SEM image of the CIS (Figure S4e) clearly demonstrates that the CIS microspheres consist of numerous petals. Similar microspheres with uniform marigold-flower-like morphologies have been reported for $CdIn_2S_4$ and $ZnIn_2S_4$.[24,45] From these results, we conclude that CIS NPs were initially formed and aggregated into the CIS spheres; these grew into petals or sheets that then self-assembled to form the uniform hierarchical marigold-flower-like morphology of the CIS microspheres.

XPS Analysis. To investigate the valence states and surface chemical composition of the CIS/TNP composites, we performed XPS analyses of the TNP, CIS, 1%-CIS/TNP, and 10%-CIS/TNP composites, and the results are shown in Figure 5 and Figure S5. The survey spectra of all of the samples show a carbon peak at a binding energy of ∼284.9−285.9 eV, derived from the carbon tape used for fixing the sample and from the adsorption of atmospheric CO_2 on the sample surface. In the CIS survey spectrum (Figure 5b), the binding energy of the oxygen peak located at 532.9 eV may be due to adsorbed H_2O and O_2 on the sample surface. In the survey spectra of all the samples, no other impurity peaks could be identified, which suggests the high purity of the obtained materials and supports the PXRD results. Figure 5c presents the high resolution XPS spectrum of Ti 2p; the peaks positioned at 459.75 and 465.20 eV are assigned to the Ti $2p_{3/2}$ and Ti $2p_{1/2}$ levels of TiO_2 and demonstrate that the valence of Ti is four. The peak at 531.03 eV corresponds to the O 1*s* level of O^{2-} in the TiO_2 (Figure S5a).[46] The CIS survey spectra (Figure 5b) reveal the presence of Ca 2p, In 3d, and S 2p in the sample. In the high-resolution Ca 2p XPS spectrum (Figure 5d), the binding energies at 342.99 and 348.99 eV with a peak splitting of 6 eV correspond to the $2p_{3/2}$ and $2p_{1/2}$ levels of the Ca^{2+} 2p orbitals. In Figure 5e, the In 3d core splits into 445.69 ($3d_{5/2}$) and 453.26 eV ($3d_{3/2}$) peaks with a peak splitting of 7.57 eV, which are consistent with the values for In^{3+}. Figure 5f shows a peak centered at 162.69 eV which is assigned to the $2p_{1/2}$ level of S^{2-} and is attributed to S coordinated to Ca and In in the CIS. The XPS results for CIS are in accord with standard reference XPS spectra, and further validate the oxidation state assignments for Ca, In, and S in the CIS marigold flowers as +2, +3, and −2, respectively.[25,26,30]

From Figure 5c and Figure S5a, we observed that the intensities of the Ti 2p and O 1s peaks decrease with increases in the CIS content, and the peak positions are shifted to higher binding energies. The decrease in the intensity and shift to higher binding energy as compared to TNP suggests the strong interaction between the TNP and CIS and validates the successful synthesis of the direct Z-scheme CIS/TNP composites. The survey spectra of the 1 and 10%-CIS/TNP composites (Figure S5b,c) reveal that the Ca, In, and S peaks are less intense with respect to the Ti and O peaks; this may be due to the lower percentage loading of CIS on TNP. However, the high-resolution XPS data clearly show the presence of Ca 2p, In 3d, and S 2p in the CIS/TNP composites, in agreement with the PXRD, FE-SEM, and TEM results. We further observed that the intensities of the Ca 2p, In 3d, and S 2p peaks increased with increases in the amounts of CIS loading, confirming the successful incorporation of the CIS and also the formation of the direct Z-scheme with TNP (Figure S5d−f). For In 3d, only one peak at a binding energy of 445.85 and 445.91 eV, corresponding to the $3d_{5/2}$ level, was observed for the 1 and 10%-CIS/TNP composites, respectively. A peak related to the $3d_{3/2}$ level of In 3d with a binding energy of 453.26 eV was not observed, which may be due to overlap with

DOI: 10.1021/acsami.5b03935
ACS Appl. Mater. Interfaces 2015, 7, 17138−17154

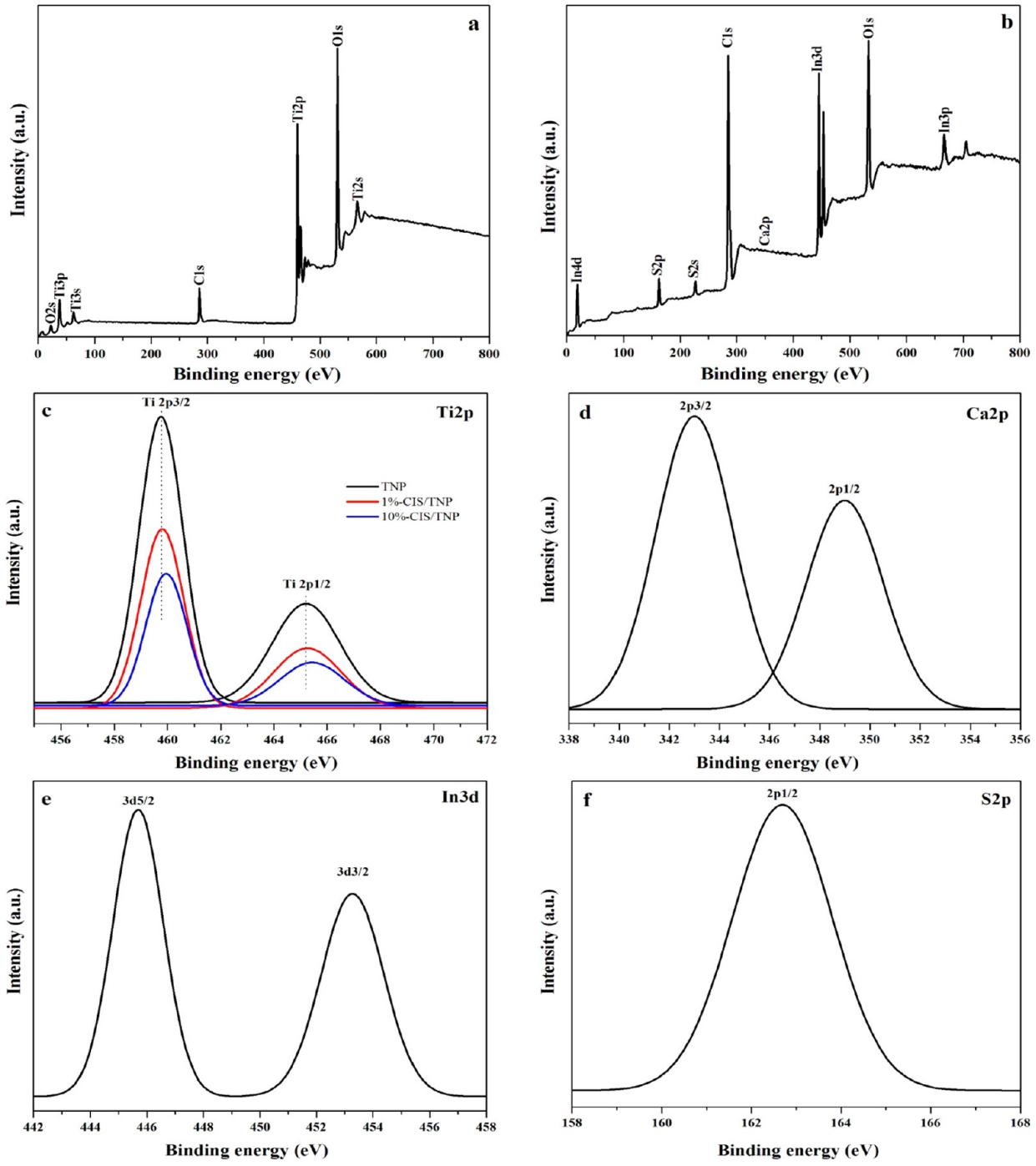

Figure 5. (a and b) XPS survey spectra of TNP and CIS, (c) high-resolution Ti 2p spectra of TNP, 1%-CIS/TNP, and 10%-CIS/TNP composites, and (d–f) high-resolution Ca 2p, In 3d, and S 2p spectra of CIS.

the Ti $2p_{3/2}$ peak in both composites. From the PXRD, FE-SEM, TEM, and XPS analyses, we conclude that the redox-mediator-free direct Z-scheme *x*%-CIS/TNP composites was successfully synthesized.

UV–Vis–DRS Analysis. The band gap energies of the CIS, TNP, and *x*%-CIS/TNP composites were determined using UV–vis–diffuse reflectance spectroscopy (UV–vis–DRS); the results are shown in Figure 6. TNP shows a broad absorbance with an absorption edge around at ~388 nm, attributed to the charge transfer from the VB to the CB of the TNP. CIS exhibits a strong and broad absorption in the visible region around 635–660 nm, indicating the intrinsic band gap transition of the $CaIn_2S_4$ rather than a transition from impurity levels.[25] From Figure 6a, we can see that the *x*%-CIS/TNP composites show two absorption edges corresponding to TNP and CIS, which increase with increasing CIS content. This could also be observed from the change of TiO_2 color from white to orange (Figure 7). The band gaps were calculated from the Kubelka–Munk function-transformed reflectance spectra (Figure 6b), and the results are shown in Table 1. The band gaps of CIS and TNP were 1.98 and 3.20 eV, respectively, whereas in the composites, the band gap of TNP was decreased with increases in the amount of CIS loading. A significant reduction in the

DOI: 10.1021/acsami.5b03935
ACS Appl. Mater. Interfaces 2015, 7, 17138–17154

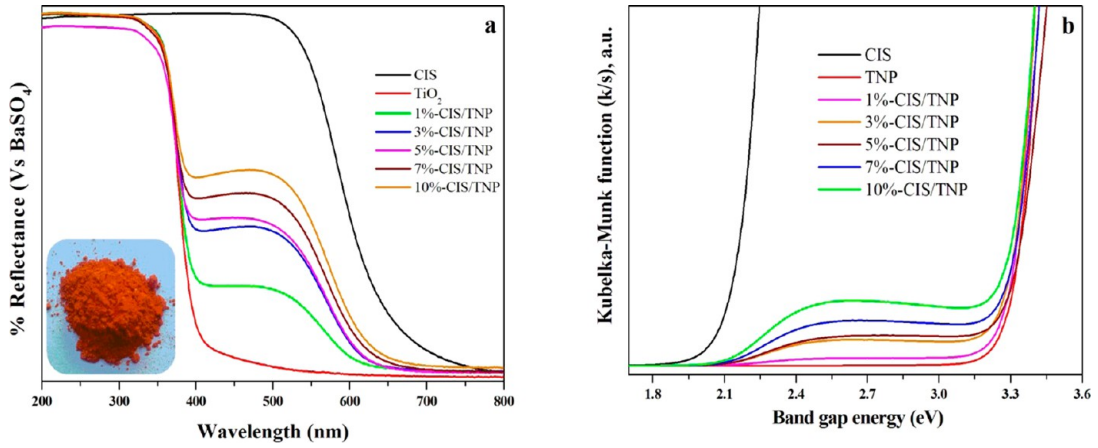

Figure 6. (a) UV−vis-DRS, (inset) orange color of the $CaIn_2S_4$ sample, and (b) Kubelka−Munk function-transformed differential spectra of CIS, TNP, and the *x*%-CIS/TNP composites.

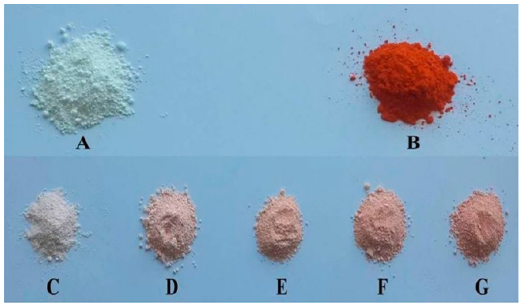

Figure 7. Photographic image of (A) TNP, (B) CIS, (C) 1%-CIS/TNP, (D) 3%-CIS/TNP, (E) 5%-CIS/TNP, (F) 7%-CIS/TNP, and (G) 10%-CIS/TNP composites.

TNP band gap would help to enhance its visible-light absorption and photocatalytic decomposition efficiency.

In the composites, the photocatalytic activity can best be explained from the VB and CB positions of the constituent semiconductors. The VB and CB positions of CIS and TNP can be calculated using the following equations.

$$E_{VB} = \chi - E_e + 0.5BG \quad (1)$$

$$E_{CB} = E_{VB} - BG \quad (2)$$

where E_{VB} and E_{CB} are the valence and conduction band potentials, respectively, BG is the band gap, χ is the geometric mean of the absolute electronegativity of the constituent atoms in the semiconductor, and E_e is the energy of free electrons on the hydrogen scale (4.5 eV vs NHE). The values of χ for TNP and CIS are 5.81 and 4.39 eV, respectively, and the data used to calculate χ for the semiconductors are tabulated in Table S2. The calculated VB and CB positions of TNP and CIS are +2.91 and −0.29 eV, and +0.88 and −1.1 eV, respectively.

Surface Area Analysis. The surface areas, pore volumes, and pore diameters of CIS, TNP, and the *x*%-CIS/TNP composites were analyzed by N_2 adsorption−desorption analysis, the results shown in Table 1. The N_2 isotherm of CIS reveals a type IV isotherm with a distinct hysteresis loop in the relative pressure (P/P_0) range of 0.45−1.0, corresponding to the mesoporous structure of CIS. Similarly, the N_2 isotherms of TNP and all the *x*%-CIS/TNP composites show typical type IV isotherms with H3-type hysteresis loops, which are usually obtained for mesoporous materials with slit-like pores (Figure S6). The surface areas and pore volumes of CIS and TNP were 93.52 and 56.74 m^2/g, and 0.081 and 0.302 cm^3/g, respectively. The surface areas of the *x*%-CIS/TNP composites increased with increases in the CIS loading, again indicating their successful syntheses. Pore size distribution analysis (Figure S7)

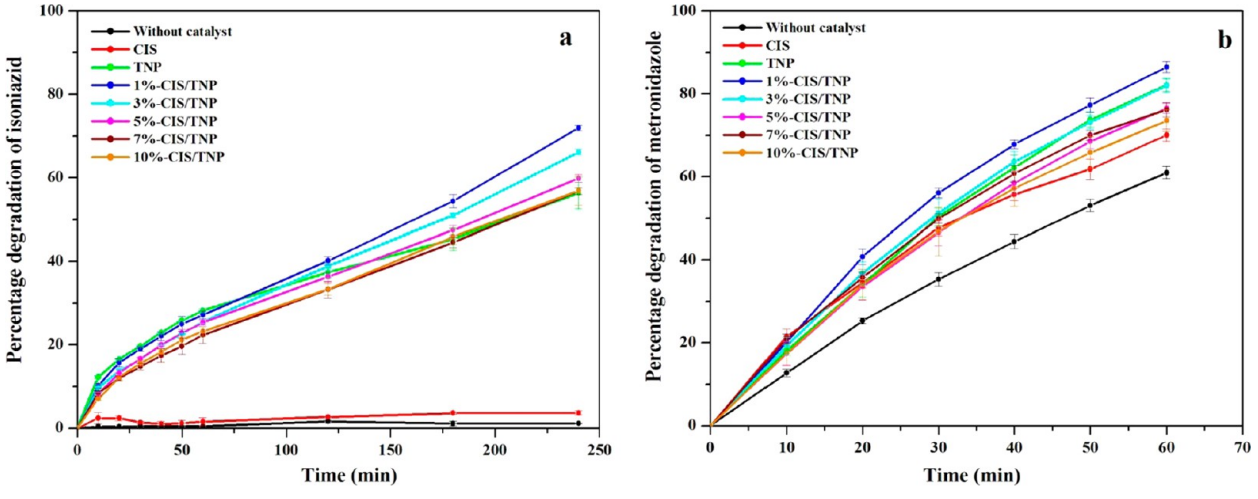

Figure 8. Percentage degradation of (a) isoniazid and (b) metronidazole using CIS, TNP, and the *x*%-CIS/TNP composites with error bar.

DOI: 10.1021/acsami.5b03935
ACS Appl. Mater. Interfaces 2015, 7, 17138−17154

revealed that the pore volume (0.302 cm^3/g) and pore diameter (21.27 nm) of TNP were reduced to 0.123 and 0.122 cm^3/g and 8.63 and 8.30 nm after the 1 and 3% loading of CIS, whereas further increases in the CIS amount (5, 7, and 10%) resulted in increasing pore volumes and diameters (Table 1). This may be because, at a lower percentage, some of the TNP pores may be blocked by the added CIS, whereas at a higher percentage loading, both the TNP and excess CIS pores are available, increasing the adsorption of N_2. The surface area analysis again supports the successful synthesis of the direct Z-scheme *x*%-CIS/TNP composites, in agreement with the preceding analyses.

Photocatalytic Activity. The photocatalytic efficiency of the synthesized CIS, TNP, and direct Z-scheme *x*%-CIS/TNP photocatalysts was evaluated through the decomposition of pharmaceutical compounds ISN and MTZ. The percentage degradation of ISN and MTZ was calculated and the results are shown in Figure 8a,b with standard error analysis. Under light irradiation alone (without catalyst, Figure 8a), 2% of the ISN was degraded, perhaps by photolysis. However, the ISN degradation process was very slow, and no apparent changes in the concentration of ISN were observed. This clearly indicates that the self-degradation of ISN is negligible in the presence of light irradiation, and further suggests that both the photocatalyst and light irradiation are necessary for the degradation to ensue. For the CIS and TNP photocatalysts (Figure 8a), 3.7 and 56.3% of the ISN was degraded after 4 h. However, with the direct Z-scheme *x*%-CIS/TNP photocatalysts, the percentage degradation of ISN was significantly enhanced. After 4 h irradiation, 71.9, 66.2, 59.8, 56.8, and 56.9% of the ISN was degraded when using the 1, 3, 5, 7, and 10%-CIS/TNP photocatalysts, respectively. The percentage degradation of ISN decreased with increasing CIS content, and the highest value was obtained with the 1%-CIS/TNP photocatalyst. The order of photocatalytic activity in ISN degradation was 1%-CIS/TNP > 3%-CIS/TNP > 5%-CIS/TNP > 7%-CIS/TNP > 10%-CIS/TNP > TNP > CIS.

For the MTZ substrate, 92% was degraded after 4 h in the presence of light irradiation (without catalyst). This indicates that, compared to ISN, MTZ is less stable under photolysis conditions. All the photocatalysts revealed enhanced photocatalytic efficiencies over the blank reaction (without catalyst). Indeed, 97% (4 h), 100% (3 h), 100% (2 h), 100% (4 h), 100% (4 h), 99% (4 h), and 99% (4 h) of the MTZ was degraded using the CIS, TNP, 1%-CIS/TNP, 3%-CIS/TNP, 5%-CIS/TNP, 7%-CIS/TNP, and 10%-CIS/TNP photocatalysts, respectively, for the given time periods. Thus, MTZ was almost completely degraded by any of the photocatalysts, and the 1%-CIS/TNP composite exhibited the highest photocatalytic activity. However, to study the influence of the added CIS on the TiO_2 photocatalyst, the degradation efficiencies were calculated for the first 1 h of reaction (Figure 8b). Without a catalyst (blank reaction), 60.9% of the MTZ was decomposed, but percentage degradation was significantly enhanced to 70, 82.1, 86.5, 81.9, 76.5, 76.2, and 73.6% in the presence of the CIS, TNP, 1%-CIS/TNP, 3%-CIS/TNP, 5%-CIS/TNP, 7%-CIS/TNP, and 10%-CIS/TNP photocatalysts, respectively. From these results, it is evident that the synthesized CIS efficiently utilizes the visible-light region of the supplied light source and enhances the visible-light photocatalytic activity of TNP. Similarly to the ISN degradation, the 1%-CIS/TNP composite photocatalyst showed higher photocatalytic activity in the degradation of MTZ than the other photocatalysts. The order of photocatalytic activity in the MTZ case was 1%-CIS/TNP > TNP > 3%-CIS/TNP > 5%-CIS/TNP > 7%-CIS/TNP > 10%-CIS/TNP > CIS. The adsorption results revealed that very small amounts of ISN and MTZ were adsorbed on the photocatalyst surface. Even though the surface area of all of the composite photocatalysts were higher than the CIS and TNP, nevertheless the percentage adsorption of ISN and MTZ was lower, suggesting that the surface area did not exert any significant effect on the photocatalytic activity of the *x*%-CIS/TNP composites. Nevertheless, the higher percentage degradation of ISN and MTZ using the 1%-CIS/TNP composite is mainly attributed to the decreased band gap as compared to TNP, which led to the absorption of the visible-light portion of the applied light source by the TNP (Figure S1). Though the other composites (3, 5, 7, and 10%-CIS/TNP) possess lower band gaps than 1%-CIS/TNP, they exhibit lower photocatalytic activity in the degradation of ISN and MTZ (Table 1). At CIS amounts exceeding 1%, the TNP surface could be completely blocked by the added CIS, and as a consequence, the intensity of the light reaching the TNP surface is significantly reduced. This was supported by the changing of the TNP color from white to orange (Figure 7). Thus, the photogeneration of active $^{\bullet}OH$ and $O_2^{\bullet-}$ species is reduced, which results in the decreased degradation of ISN and MTZ. Hence, the *x*%-CIS/TNP photocatalyst with 1% CIS is optimal for improved photocatalytic performance in the degradation of ISN and MTZ using the current reaction conditions. Standard error analysis also reveals the reproducibility of the results.

To confirm the degradation of ISN and MTZ, COD analysis was performed on the photodegraded samples. In the CIS-only and blank (without catalyst) reactions, no reductions in the COD values were observed for the ISN reaction samples, whereas COD was reduced by 45, 70.1, 61.2, 53.4, 50.6, and 47.4% in the presence of the TNP, 1%-CIS/TNP, 3%-CIS/TNP, 5%-CIS/TNP, 7%-CIS/TNP, and 10%-CIS/TNP photocatalysts, respectively. In the case of MTZ, 33.7 and 43.4% of the COD was reduced in the blank and CIS-mediated photocatalytic reactions, although 60.9 and 70% of the MTZ was degraded after UV analysis. Nevertheless, the COD analysis revealed that MTZ was degraded into intermediate products. The 43.4% COD reduction in the presence of the CIS photocatalyst further evidence that the visible-light region of the light source could be effectively utilized by CIS, which would enhance the visible-light response of TNP. The percentage reductions in the COD when using the TNP, 1%-CIS/TNP, 3%-CIS/TNP, 5%-CIS/TNP, 7%-CIS/TNP, and 10%-CIS/TNP photocatalysts were 78.3, 82.8, 77.4, 72.8, 70.5, and 68.2%, respectively. The percentage reduction of COD for both the ISN and MTZ degradation using optimized 1%-CIS/TNP photocatalyst were 70.1 and 82.8% respectively. The reductions in COD values for both the ISN and MTZ degradations agree with the degradation percentage results attained from the UV−vis spectroscopic analysis. Thus, we conclude that the presence of CIS promotes significant improvement in the photocatalytic performance of TNP.

The enhanced photocatalytic activity of the direct Z-scheme 1%-CIS/TNP photocatalyst on the degradation of ISN and MTZ can be explained by the Langmuir−Hinshelwood mechanism. The plot of ln C_0/C_t versus t affords a straight line, suggesting that the degradations of ISN and MTZ by all the catalysts follow pseudo-first-order kinetics. Moreover, the regression coefficient values (R^2 = 0.9) show that the ISN and MTZ degradations by all the photocatalysts fit the Langmuir−

DOI: 10.1021/acsami.5b03935
ACS Appl. Mater. Interfaces 2015, 7, 17138−17154

Hinshelwood kinetic model. The initial rates and rate constants for the ISN and MTZ degradation reactions were calculated, and the results are given in Table 2. Kinetic analysis revealed

Table 2. Kinetic Analysis Data for the Photocatalytic Degradation of ISN and MTZ

	isoniazid (ISN)		metronidazole (MTZ)	
photocatalyst	initial rate, $\times 10^{-6}$ (mol L^{-1} min^{-1})	rate constant, k, $\times 10^{-3}$ (min^{-1})	initial rate, $\times 10^{-6}$ (mol L^{-1} min^{-1})	rate constant, k, $\times 10^{-2}$ (min^{-1})
CIS	0.15	0.41	4.89	1.61
TNP	2.26	6.26	5.38	1.77
1%-CIS/TNP	2.33	6.49	5.79	1.91
3%-CIS/TNP	1.96	5.50	5.54	1.82
5%-CIS/TNP	1.91	5.36	5.04	1.66
7%-CIS/TNP	1.57	4.40	5.07	1.67
10%-CIS/TNP	1.78	4.97	5.32	1.75

that the direct Z-scheme 1%-CIS/TNP photocatalyst afforded higher initial rates for both ISN (2.33×10^{-6} mol L^{-1} min^{-1}) and MTZ (5.79×10^{-6} mol L^{-1} min^{-1}) degradation than the other photocatalysts. These kinetic studies confirmed that the direct Z-scheme 1%-CIS/TNP composite displays enhanced photocatalytic efficiency for ISN and MTZ degradation under the current reaction conditions, in support of the UV results.

Photocatalytic Mechanism. The photocatalytic efficiency of a system relies primarily on the rate of recombination of the photogenerated electron−hole pairs, as well as the production and participation of active radical species. To ascertain the enhancement in the photocatalytic activity of 1%-CIS/TNP photocatalyst relative to the other composites, TNP, and CIS in the degradation of ISN and MTZ, we determined the recombination behavior of the photogenerated charge carriers and the contribution of radical species in the reaction using photoluminescence (PL) analysis and radical-trapping experiments, respectively. These results were then correlated with the photocatalytic efficiency and proposed the mechanism.

The intensity of a PL spectrum can be correlated with the recombination rate of the photogenerated electron−hole pairs. A lower PL intensity may signify that the rate of recombination is lower, which increases the lifetimes of the charge carriers and the photocatalytic degradation efficiency. The reverse case would lead to lower photocatalytic activity. The PL spectra of the CIS, TNP, and x%-CIS/TNP Z-scheme photocatalysts were recorded at excitation wavelength of 330 nm, and the results are presented in Figure 9. TNP shows emissions at 384, 415, 469, and 508 nm. At 330 nm excitation, CIS does not show any apparent emission peaks, but the emission at 384 nm may be due to the radiative annihilation of the photoexcited electrons in the CB with the holes in the VB of TNP. The emissions at 415, 469, and 508 nm are attributed to surface state emissions. Such emissions occur mainly because of the presence of surface defects or oxygen vacancies associated with the Ti^{3+} in anatase TiO_2.[47−54] From Figure 9, we can see that the PL intensities of the direct Z-scheme x%-CIS/TNP photocatalysts are lower than those of TNP, suggesting that these composite materials have lower recombination rates.

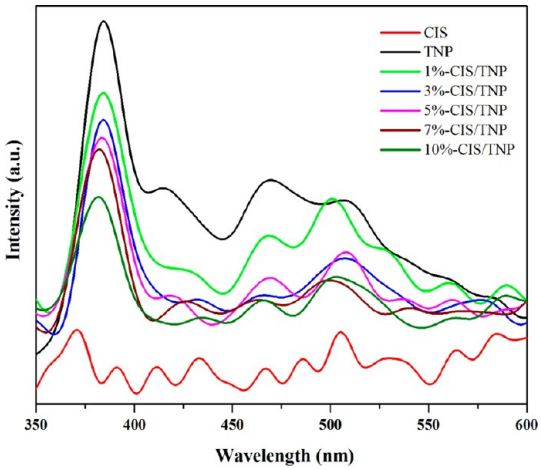

Figure 9. PL spectra of CIS, TNP, and the x%-CIS/TNP composites at 330 nm excitation wavelength.

Moreover, the PL intensities decrease with the increase in the CIS content, indicating that the recombination rate of charge carriers is lower than the TNP. Among the x%-CIS/TNP composites, 1%-CIS/TNP exhibited higher photocatalytic efficiency than the other composites and TNP. Although the PL intensities of the other composites were lower than that of 1%-CIS/TNP, they nevertheless showed lower photocatalytic efficiency. This is because, when the amount of CIS exceeds 1%, the TiO_2 surface is totally occluded by the added CIS and the intensity of the light reaching the TNP is reduced. Therefore, the generation of the active $^{\bullet}OH$ and $O_2^{\bullet-}$ radicals is decreased, which results in the reduced photodegradation of ISN and MTZ at higher percentages of CIS. From the PL analysis, we can conclude that the recombination rate of the charge carriers was efficiently decreased after forming the TNP composites with CIS. The electron−hole transfer mechanism and the enhanced photocatalytic degradation efficiency of 1%-CIS/TNP were further confirmed by radical trapping experiments, hydroxyl ($^{\bullet}OH$) radical determination, photocurrent, and electron spin resonance (ESR) analysis.

The photocatalytic degradation of pollutants occurs mainly through the involvement of photogenerated holes (h^+), hydroxyl ($^{\bullet}OH$) radicals, and superoxide ($O_2^{\bullet-}$) radical anions. To determine the radicals involved in the reaction and the mechanism underlying the enhanced photocatalytic activity of 1%-CIS/TNP, radical trapping experiments were performed. In this study, the scavengers AO, IPA, and BQ were used to scavenge the h^+, $^{\bullet}OH$, and $O_2^{\bullet-}$ species in the photocatalytic processes, respectively. The effects of different scavengers on the degradation efficiency of ISN and MTZ are shown in Figure 10a,b. The results revealed that the percentage degradation of ISN was dramatically decreased to 14.3, 29.5, and 30.2% after the addition of AO, IPA, and BQ, respectively, as compared to 71.9% in the absence of the scavengers (Figure 10a). Similarly, the percentage degradation of MTZ was decreased from 86.5% (no scavenger) to 67.1% (AO), 52.4% (IPA), and 53.2% (BQ; Figure 10b). We infer that h^+, $^{\bullet}OH$, and $O_2^{\bullet-}$ radicals play equally vital role in the photocatalytic degradation reaction. According to these results, the main reactive species participated in the photocatalytic degradation of ISN and MTZ over the 1%-CIS/TNP photocatalyst are h^+, $^{\bullet}OH$, and $O_2^{\bullet-}$.

DOI: 10.1021/acsami.5b03935
ACS Appl. Mater. Interfaces 2015, 7, 17138−17154

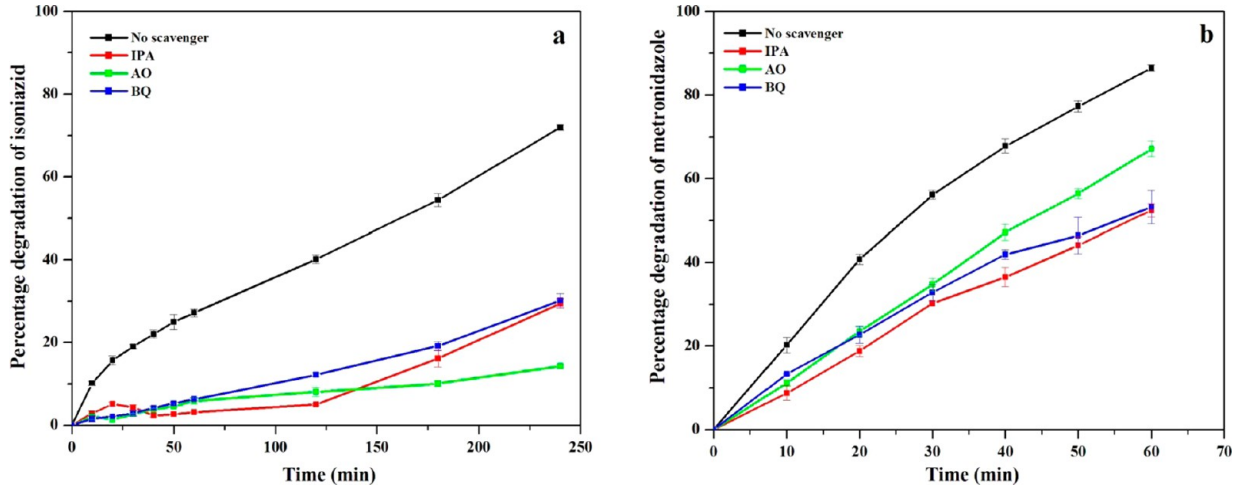

Figure 10. Effect of scavengers on the percentage degradation of (a) isoniazid and (b) metronidazole using direct Z-scheme 1%-CIS/TNP photocatalyst with error bar.

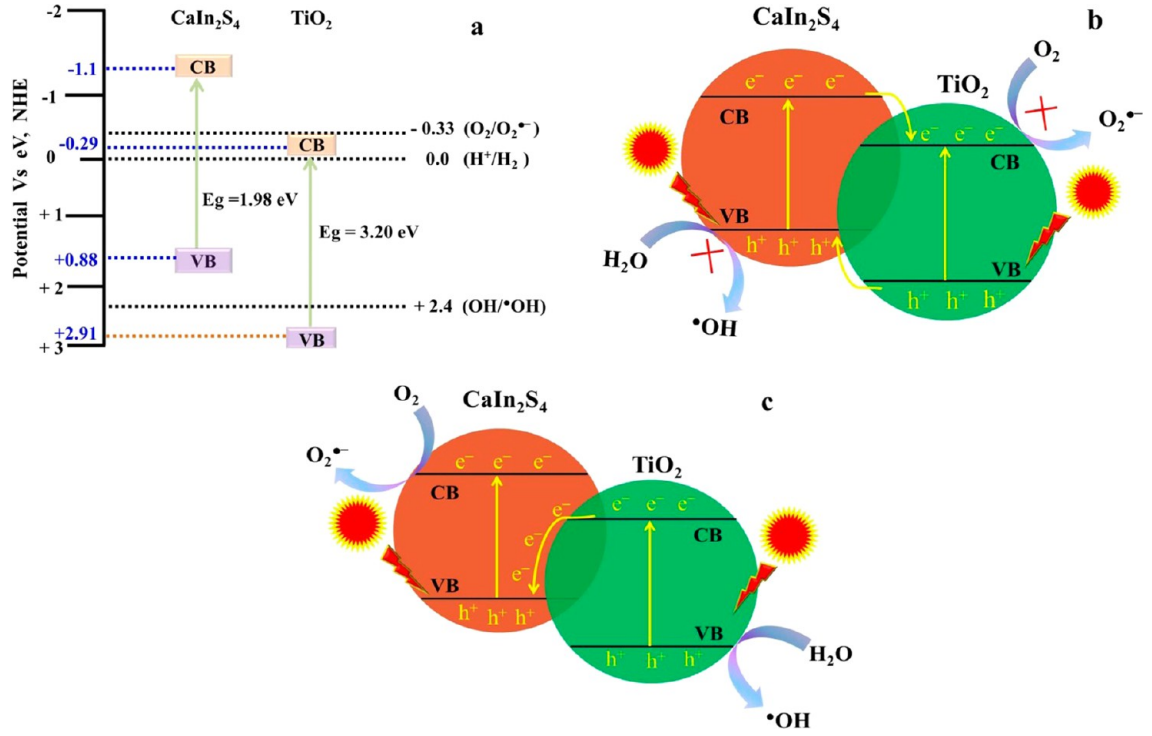

Figure 11. Schematic representation of (a) the band positions of CIS and TNP, and (b and c) heterojunction and Z-scheme-type electron−hole transfer mechanisms.

From the foregoing results and the band gap structures of CIS and TNP, a possible mechanism for the enhanced photocatalytic activity of the 1%-CIS/TNP Z-scheme photocatalyst was proposed and is schematically represented in Figure 11. The calculated VB and CB positions of TNP and CIS are shown in Figure 11a. Under irradiation, both TNP and CIS absorb light, and excitation of the electrons to the CBs of both TNP and CIS creates holes in the VBs. If the coupling of CIS and TNP forms a heterojunction-type photocatalyst, then photogenerated electrons and holes transfer processes occur, as shown in Figure 11b, which is the common charge carrier separation process for a large number of composite photocatalysts.

The charge carriers are separated by the migration of the electrons from the CB of the CIS to the CB of the TNP, while holes in the VB of TNP simultaneously migrate into the VB of CIS. This can offer the efficient separation of the photogenerated electrons and holes. However, the accumulated holes on the VB of CIS cannot produce $^{\bullet}OH$ radicals by the oxidization of surface hydroxyl groups or adsorbed water molecules. Similarly, the electron on the CB of TNP cannot reduce oxygen molecules (O_2) into superoxide radicals ($O_2^{\bullet-}$). Because the CB potential of TNP (−0.29 eV vs NHE) is more positive than the redox potential of $O_2^{\bullet-}$ formation ($O_2/O_2^{\bullet-}$ = −0.33 eV vs NHE) and the VB potential of the CIS (+0.88 eV vs NHE) is more negative than the potential required to oxidize H_2O or −OH to $^{\bullet}OH$ radicals (+2.4 eV vs NHE). Therefore, if

DOI: 10.1021/acsami.5b03935
ACS Appl. Mater. Interfaces 2015, 7, 17138−17154

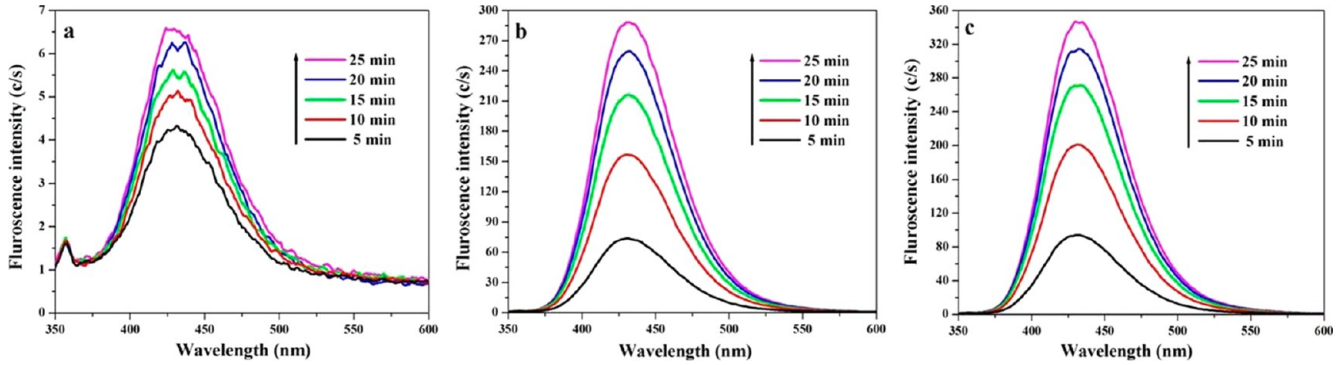

Figure 12. Fluorescence spectral changes observed during irradiation of the (a) CIS, (b) TNP, and (c) 1%-CIS/TNP sample in a 5×10^{-4} M basic solution of terephthalic acid (excitation at 315 nm).

the charge carriers transfer follows the heterojunction (Figure 11b), then it is not encouraging the production of the main reactive species ($^{\bullet}OH$, and $O_2^{\bullet-}$) and decreased the photocatalytic decomposition efficiency of CIS/TNP composites. However, the degradation results demonstrated that reactive species show higher oxidizability and reducibility in the reaction and increased the photocatalytic activity. Therefore, the photogenerated electron−hole pair separation process follows the Z-scheme mechanism, as shown in Figure 11c. It is well supported by radical-trapping experiments (Figure 10) that the percentage of degradation of ISN and MTZ was dramatically decreased after the addition of AO and IPA scavengers. From these results, it can be evidently suggested that photogenerated holes are actively involved in the reaction and yielded higher concentration of $^{\bullet}OH$ radicals. In the Z-scheme mechanism, the photogenerated electrons in the CB of TNP are transferred to the VB of the CIS, where they recombine with holes in the VB of the CIS. Consequently, the electrons in the CB of the CIS and the holes in the VB of the TNP are well separated, which effectively participate in the reaction to produce a higher quantities of $^{\bullet}OH$ and $O_2^{\bullet-}$ and enhances the photocatalytic activity of CIS/TNP composites. Because the higher positive VB potential of TNP (+2.91 eV) oxidizes the surface hydroxyl groups or adsorbed water molecules to $^{\bullet}OH$ radicals (H_2O or $-OH/^{\bullet}OH$ = +2.4 eV vs NHE). Similarly, the higher negative CB potential of CIS (−1.1 eV) reduces O_2 to $O_2^{\bullet-}$ ($O_2/O_2^{\bullet-}$ = −0.33 eV vs NHE). The higher amounts of $^{\bullet}OH$ and $O_2^{\bullet-}$ radicals would lead to higher oxidation/reduction abilities in the CIS/TNP composite, which would result in enhanced photocatalytic performance as compared to the individual CIS and TNP photocatalysts. Similar Z-scheme transfer of photogenerated charge carriers and its supporting evidence by radical scavenging studies has been reported for various direct Z-scheme photocatalysts such as g-C_3N_4/TiO_2, $NaNbO_3$/WO_3, WO_3/g-C_3N_4, BiOCl/g-C_3N_4, Bi_2O_3/g-C_3N_4, Bi_2O_3/$NaNbO_3$, $BiVO_4$/g-C_3N_4, Ag_3PO_4/g-C_3N_4, SnO_{2-x}/g-C_3N_4, and α-Fe_2O_3/Cu_2O.[55−64] The PL analysis results further support the superior photocatalytic efficiency of the direct Z-scheme CIS/TNP photocatalysts (Figure 9). At 330 nm excitation (Figure 9), the PL intensities of the *x*%-CIS/TNP composites are lower than that of TNP indicating slower recombination rates. This clearly suggests that after forming a direct Z-scheme between the TNP and CIS, the recombination rates on the TNP surface are significantly suppressed, which increases the photocatalytic activity. This validates that the electron−hole transfer process follows the Z-scheme mechanism shown in Figure 11c and proves the successful formation of the redox-mediator-free direct Z-scheme between these two semiconductors. Thus, it shows a significantly improved photocatalytic activity for the CIS/TNP composites under light irradiation. However, the 1%-CIS/TNP composite showed higher photocatalytic activity than the TNP and other composites, and therefore, 1% CIS appears to be the optimum loading for enhancing photocatalytic efficiency. Overall, we conclude that the superior photocatalytic performance of 1%-CIS/TNP is mainly due to the efficient separation of charge carriers by following the Z-scheme mechanism, as shown in Figure11c. Further confirmation of Z-scheme transfer of charge carriers was carried out by hydroxyl ($^{\bullet}OH$) radicals formation determination studies and photocurrent and ESR analyses.

Evidence of the Mechanism. *Hydroxyl Radical Determination.* The enhanced photocatalytic activity of 1%-CIS/TNP composite and the direct Z-scheme principled mechanism of photogenerated charge carriers transfer were further confirmed by hydroxyl radicals ($^{\bullet}OH$) determination using fluorescence spectroscopy and terephthalic acid (TA) as a probe molecule. It is well-known that fluorescence intensity corresponds to the concentration of $^{\bullet}OH$ radicals; thus, higher the fluorescence intensity results generation of large number of $^{\bullet}OH$ radicals in a particular reaction.[40] The $^{\bullet}OH$ radical determination reaction using CIS, TNP, and 1%-CIS/TNP photocatalysts were performed, and the results are shown in Figure 12. The results reveal that in all the photocatalytic system fluorescence intensity is increased with increase in the irradiation time (Figure 12a−c). It is suggested that $^{\bullet}OH$ radicals are formed in the photocatalytic degradation reaction, which agrees well with the results of $^{\bullet}OH$ radicals quenching by IPA. However, the 1%-CIS/TNP composite shows higher fluorescence intensity results, and the formation rate of $^{\bullet}OH$ radicals on this surface is much higher than that of the CIS and TNP photocatalyst. This should be ascribed to the Z-scheme charge carrier transfer over 1%-CIS/TNP photocatalyst,[59,60] consequence enhancements of holes on the VB of TNP to produce higher concentration of $^{\bullet}OH$ radicals and yielded higher fluorescence intensity than the CIS and TNP. We infer that 1%-CIS/TNP composite surface is more suitable for generation of higher number $^{\bullet}OH$ radicals, which leads to the higher percentage degradation of ISN and MTZ pharmaceuticals (Figure 8a,b). Whereas, in the case of TNP photocatalyst, low fluorescence intensity was observed due to the lower formation rate of $^{\bullet}OH$ radicals (Figure 12b) and showed less percentage degradation of ISN and MTZ. Moreover, the very low fluorescence intensity of CIS (Figure 12a) suggested that negligible amount of $^{\bullet}OH$ radicals were formed on its surface.

DOI: 10.1021/acsami.5b03935
ACS Appl. Mater. Interfaces 2015, 7, 17138−17154

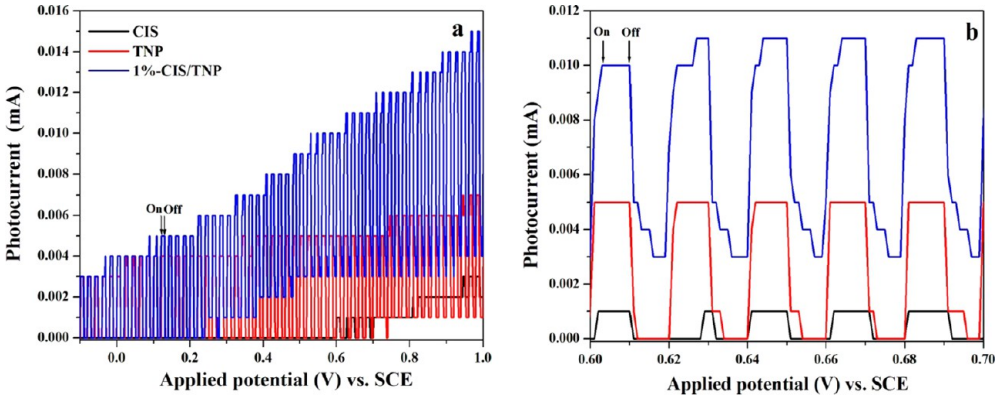

Figure 13. (a) Chopping visible-light photocurrent−voltage curves for CIS, TNP and 1%-CIS/TNP composites in 0.1 M Na_2SO_4 aqueous solution and (b) the curves expanded in the range of 0.6−0.7 V.

This may be due to the reaction of formed superoxide radicals with water. It proves that lower VB potential of CIS cannot generate $^{\bullet}OH$ radicals by the reaction of photogenerated holes with water and displayed very less fluorescence intensity (Figure 12a). Therefore, if both the TNP and CIS form a heterojunction type photocatalyst then the accumulated photogenerated holes on the VB of CIS cannot produce a $^{\bullet}OH$ radicals for degradation. This result evidently confirms that photogenerated electrons and holes in the CIS/TNP composites are well separated in the CB and VB of the CIS and TNP by following the Z-scheme mechanism, which results in the higher formation rate of $^{\bullet}OH$ radicals over the 1%-CIS/TNP sample and shows higher fluorescence intensity (Figure 12c) and photocatalytic activity than those of the TNP and CIS photocatalysts. From these results, we further observed that $^{\bullet}OH$ radicals are one of the prime reactive radical species for the higher photocatalytic decomposition efficiency of 1%-CIS/TNP composite and support the radical scavenging studies results (Figure 10). From these reactive species, scavenging and $^{\bullet}OH$ radicals determination studies evidently proved that photogenerated electron−hole transfer on the 1%-CIS/TNP composite follow the Z-scheme mechanism as shown in Figure 11c.

Photocurrent Measurement. To further prove the efficient separation of photogenerated charge carriers in the synthesized CIS/TNP composites, we carried out photocurrent measurements of CIS, TNP, and 1%-CIS/TNP samples in several on−off intermittent irradiation cycles, and the results are shown in Figure 13. The results revealed that photocurrent intensity was remained higher when the light was on, and it quickly decreased to zero when the light was off. Furthermore, 1%-CIS/TNP composite showed about 10 and 2 times higher photocurrent response than the CIS and TNP photocatalyst, respectively. This result is consistent with the PL analysis. The increased photocurrent response of 1%-CIS/TNP suggested that photogenerated electron−hole pairs are highly separated and decreased their recombination rate under light irradiation. This result corroborates that charge carriers transfer process over the CIS/TNP composite photocatalyst could be attributed to the Z-scheme transfer, yielded higher concentration of holes in the CIS/TNP composite, which leads to the production of higher concentration of $^{\bullet}OH$ radicals (Figure 12c) and enriched the photocatalytic activity in degradation of ISN and MTZ. Similar enhanced photocurrent response through the effective separation of electrons and holes by following the Z-scheme transfer were reported in the direct Z-scheme $BiVO_4$/g-C_3N_4,[61] SnO_{2-x}/g-C_3N_4,[63] and α-Fe_2O_3/Cu_2O[64] photocatalysts. This was further supported by reactive species quenching studies, the percentage degradation of ISN and MTZ was drastically decreased after the addition of AO and IPA (Figure 10). From the Results and Discussion, it is apparent that transfer of photogenerated charge carriers in the CIS/TNP composite photocatalyst follows the mechanism presented in Figure 11c and the CIS/TNP composites are indeed typical direct Z-scheme photocatalysts.

Electron Spin Resonance (ESR) Measurement. To validate the proposed mechanism for separation of photogenerated electrons and holes on the CIS/TNP composite, we carried out ESR experiments of CIS, TNP, and 1%-CIS/TNP. ESR analysis was performed as follows 10 μL of DMPO and 0.25 mL of methanol were added into 5 mg of samples separately, sonicated and irradiated for 300 s. Subsequently, this methanol dispersion was used for the detection of $O_2^{\bullet-}$ radicals and the results were shown in Figure 14. The results revealed that there

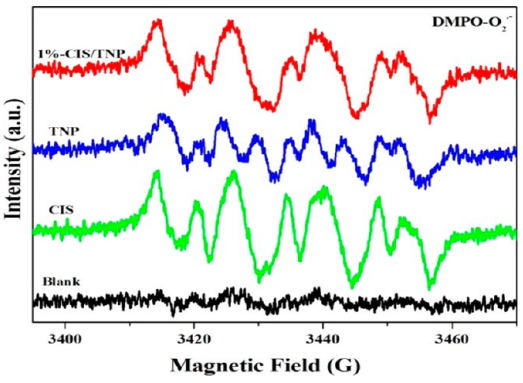

Figure 14. ESR signals of the DMPO-$O_2^{\bullet-}$ with irradiation for 300 s in methanol dispersion (blank = methanol dispersion without photocatalyst).

were no DMPO-$O_2^{\bullet-}$ adducts under blank condition, and thus, we infer that $O_2^{\bullet-}$ radicals were generated only in the presence of photocatalysts. In the ESR patterns of the CIS, TNP and 1%-CIS/TNP samples show six characteristic peaks of the DMPO-$O_2^{\bullet-}$ adducts, proving that $O_2^{\bullet-}$ radicals have been generated during the photocatalytic degradation reaction. Moreover, the intensity of these characteristic peaks of DMPO-$O_2^{\bullet-}$ adducts in 1%-CIS/TNP sample is higher than that of the TNP sample. This suggests that the concentration of $O_2^{\bullet-}$ radicals on the surface of 1%-CIS/TNP is higher than that of TNP. It evidently

DOI: 10.1021/acsami.5b03935
ACS Appl. Mater. Interfaces 2015, 7, 17138−17154

Table 3. Comparison of Degradation Percentages of Metronidazole (MTZ) with Literature

sample no.	catalyst	light source	concentration (mg/L) and volume (mL) of MTZ	catalyst amount (mg)	degradation (%)	illumination time (min)	ref
1	Ag-doped TiO_2, CdS, ZnS	HPMV lamp (125 W)	15 and −	0.5 g/L	94.39 (1% Ag−TiO_2) 95.11 (1.5% Ag−CdS) 94.9 (1.25% Ag−ZnS)	120	32
2	Zn_2GeO_4 HS	UV light (20 W)	10 and 100	100	100	80	33
3	$ZnSnO_3$ HNS/RGO	U-shaped xenon lamp (500 W)	5 and 200	200	72.5	180	34
4	ZnO/RGO	HPMV lamp (300 W)	5 and 200	200	49.3	160	35
5	$BiVO_4$ microcolumns	U-shaped xenon lamp (500 W)	20 and 150	150	70	180	36
6	$BiVO_4/FeVO_4$	Xe lamp (500 W)	10 and 50	200	91	90	37
7	CdS/g-C_3N_4	Xe lamp (500 W)	5 and 400	400	98	300	38
8	1%-CIS/TNP	HPMV lamp (200 W)	50 and 500	100	100	120	this study

*RGO, reduced graphene oxide; HS, hollow sphere; HNS, hollow nanosphere; HPMV, high-pressure mercury lamp; −, no data available.

proves the formation of Z-scheme between CIS and TNP; subsequently, electrons in the CB of TNP migrate to the VB of CIS and recombine with the holes in the VB of CIS. Afterward, the photogenerated electrons and holes in the CB and VB of the CIS and TNP were effectively separated, as shown in Figure 11c, and involved in the reduction and oxidation of O_2 and −OH to $O_2^{\bullet-}$ and $^{\bullet}OH$ radicals. Moreover, 1%-CIS/TNP sample shows lower peak intensity than the bare CIS because, under reaction conditions, some of the produced $O_2^{\bullet-}$ radicals were transferred into $^{\bullet}OH$ radicals, which supports the fluorescence spectroscopy results (Figure 12c). Furthermore, the higher intensity of DMPO-$O_2^{\bullet-}$ adducts in CIS samples suggested that CB position of CIS possesses sufficient negative potential to reduce the molecular oxygen to $O_2^{\bullet-}$ radicals. Similar results were obtained for $NaNbO_3/WO_3$,[56] Bi_2O_3/g-C_3N_4,[59] $Bi_2O_3/NaNbO_3$,[60] Ag_3PO_4/g-C_3N_4,[62] and N-doped ZnO/g-C_3N_4[65] core−shell nanoplates direct Z-scheme photocatalysts. From the aforementioned reactive radicals quenching, hydroxyl radical determination, band gap structures of CIS and TNP, and photocurrent and ESR analyses, we conclude that the photogenerated electron and hole transfer follows the Z-scheme mechanism (Figure 11c) and supports the enhanced photocatalytic decomposition efficiency of $CaIn_2S_4$ marigold-flower-like/TiO_2 photocatalyst in the degradation of ISN and MTZ using our current experimental conditions.

Reusability of the Photocatalyst. Reusability of the photocatalyst is one of the most important factors in catalysis research and for practical application. To evaluate the reusability and higher photocatalytic performance of 1%-CIS/TNP, the degradation reaction of ISN and MTZ were performed up to five cycles. The results revealed that there was no obvious loss of percentage degradation of ISN and MTZ after five cycles of degradation experiment using 1%-CIS/TNP sample (Figure S8a,b). However, the slight decrease in the percentage degradation after the third cycle may be due to the loss of photocatalyst during the cycling experiment. Moreover there was no change in the PXRD patterns of the used and fresh photocatalyst (Figure S8c), indicating that photocatalyst is highly stable under our photocatalytic degradation experiment condition and retain its degradation performance.

Comparison of Photocatalytic Efficiency of Present System with Literature. Generally, photocatalytic decomposition efficiency of any photocatalyst system is mainly dependent on experimental conditions such as light source, concentration and volume of pollutants, amount of photocatalyst, and irradiation time. In this work, to the best of our knowledge, we have developed a novel redox-mediator-free direct Z-scheme $CaIn_2S_4$ marigold-flower-like/TiO_2 photocatalyst for the degradation of ISN and MTZ pharmaceuticals. To justify the superior photocatalytic efficiency of the present system, we have compared with earlier reported work on the photocatalytic degradation of ISN and MTZ. It is understood that only one study is available on the degradation of ISN using Degussa P25 TiO_2 (P25) and ZnO photocatalyst.[39] The results demonstrated that 94% ISN was degraded after 300 min using P25; however, in our system 71.9% of ISN was degraded after 240 min. It seems that the reported system is more efficient than our system; however, in the reported system, the concentration of ISN (10 mg/L) is very low, and the amount of photocatalyst (1g/L) and time of irradiation (300 min) used for degradation higher than those of our catalytic system (50 mg/L of ISN, 0.2 g/L of photocatalyst, 240 min). It is clearly suggested that present redox-mediator-free direct Z-scheme $CaIn_2S_4$ marigold-flower-like/TiO_2 photocatalyst is more efficient than the reported literature in degradation of ISN. For MTZ degradation, the photocatalytic activity was compared with the reported literature, and the results are tabulated in Table 3. Similar to ISN degradation, the higher amount of photocatalyst has been used for the degradation of very low concentration of MTZ, and degradation reactions were performed using low volume of MTZ solution. However, in our catalytic system, we have used a lesser amount of photocatalyst for the degradation of higher concentration and volume of MTZ. The treatment of higher concentration and volume of pollutants using less photocatalyst will reduce needless waste. Subsequently, this will be very helpful for the treatment of industrial wastewater with low cost and energy utilization, which is one of the most important features of green chemistry. Therefore, the higher photocatalytic activity of 1%-CIS/TNP can be attributed to the efficient separation of photogenerated electron−hole pairs by Z-scheme mechanism. From the aforementioned comparative results, we infer that redox-mediator-free direct Z-scheme $CaIn_2S_4$ marigold-flower-like/TiO_2 photocatalyst may be a superior photocatalyst than the reported system for the degradation of ISN and MTZ using our current experimental conditions.

DOI: 10.1021/acsami.5b03935
ACS Appl. Mater. Interfaces 2015, 7, 17138−17154

CONCLUSION

Novel redox-mediator-free direct Z-scheme $CaIn_2S_4$ marigold-flower-like/TiO_2 photocatalysts were synthesized. Uniform hierarchical marigold-flower-like $CaIn_2S_4$ microspheres were obtained through the formation and aggregation of nanoparticles, followed by the growth and subsequent self-assembly of petals or sheets. The firm, intimate contact between the $CaIn_2S_4$ marigold flowers and TiO_2 in the Z-scheme photocatalyst was confirmed by PXRD, FE-SEM, TEM, XPS, and UV−vis-DRS analyses. The photocatalytic activity results demonstrated that the direct Z-scheme $CaIn_2S_4$ marigold-flower-like/TiO_2 photocatalysts showed relatively improved photocatalytic performance in the degradation of ISN and MTZ over the individual $CaIn_2S_4$ and TiO_2 materials. The order of photocatalytic activity for ISN degradation was 1%-CIS/TNP > 3%-CIS/TNP > 5%-CIS/TNP > 7%-CIS/TNP > 10%-CIS/TNP > TNP > CIS, and for MTZ, 1%-CIS/TNP > TNP > 3%-CIS/TNP > 5%-CIS/TNP > 7%-CIS/TNP > 10%-CIS/TNP > CIS. Hence, a 1% loading of $CaIn_2S_4$ was the optimum percentage for enhanced photocatalytic activity. Radical-trapping experiments, hydroxyl radical determination studies, and photocurrent and ESR analyses proved that the considerably enhanced photocatalytic efficiency could be ascribed to a Z-scheme-type migration of the photogenerated charge carriers. ISN and MTZ degradation was confirmed using kinetic studies and COD analyses. These results also concluded that the redox-mediator-free direct Z-scheme $CaIn_2S_4/TiO_2$ photocatalyst is a superior photocatalyst for the degradation of the ISN and MTZ pharmaceutical compounds under the given reaction conditions.

ASSOCIATED CONTENT

Supporting Information

Chemicals and materials, photocatalysts characterization details, spectral distribution of the light source, FE-SEM and TEM analyses of CIS, FE-SEM-EDX and elemental mapping analyses of 10%-CIS/TNP, XPS survey and high-resolution spectra of 1 and 10%-CIS/TNP, surface area and pore size distribution analysis results, calculation of VB and CB positions of CIS and TNP, and recyclability test of 1%-CIS/TNP photocatalyst. The Supporting Information is available free of charge on the ACS Publications website at DOI: 10.1021/acsami.5b03935.

AUTHOR INFORMATION

Corresponding Author

*E-mail: tsknatarajan@gmail.com, organthillai@gmail.com.

Notes

The authors declare no competing financial interest.

ACKNOWLEDGMENTS

The authors are thankful for the National Research Foundation of Korea (NRF) grant funded by the Korean Government (MEST) (No. 2011-0027916) for financial assistance. We also thank Dr. S. Shin, Mr. Joon Y. Lee, Mr. Sang Woo Kim, Miss Mi-Gyeong Kim, and Mr. Kong Jung Tae for their kind support. We also thank the reviewers of this manuscript for their useful comments and valuable suggestions to improve the quality of manuscript.

REFERENCES

(1) Hoffmann, M. R.; Martin, S. T.; Choi, W.; Bahnemann, D. W. Environmental Applications of Semiconductor Photocatalysis. *Chem. Rev.* **1995**, *95*, 69−96.
(2) Lee, S. K.; Mills, A. Detoxification of Water by Semiconductor Photocatalysis. *J. Ind. Eng. Chem.* **2004**, *2*, 173−187.
(3) Chen, X.; Mao, S. S. Titanium Dioxide Nanomaterials: Synthesis, Properties, Modification, and Applications. *Chem. Rev.* **2007**, *107*, 2891−2959.
(4) Dalrymple, O. K.; Yeh, D. H.; Trotz, M. A. Removing Pharmaceuticals and Endocrine-Disrupting Compounds from Wastewater by Photocatalysis. *J. Chem. Technol. Biotechnol.* **2007**, *82*, 121−134.
(5) Jo, W. K.; Kim, J. T. Application of Visible-light Photocatalysis with Nitrogen-doped or Unmodified Titanium Dioxide for Control of Indoor-level Volatile Organic Compounds. *J. Hazard. Mater.* **2009**, *164*, 360−366.
(6) Jo, W. K.; Won, Y.; Hwang, I.; Tayade, R. J. Enhanced Photocatalytic Degradation of Aqueous Nitrobenzene Using Graphitic Carbon−TiO_2 Composites. *Ind. Eng. Chem. Res.* **2014**, *53*, 3455−3461.
(7) Chen, X.; Shen, S.; Guo, L.; Mao, S. S. Semiconductor-based Photocatalytic Hydrogen Generation. *Chem. Rev.* **2010**, *110*, 6503−6570.
(8) Izumi, Y. Recent Advances in the Photocatalytic Conversion of Carbon Dioxide to Fuels with Water and/or Hydrogen using Solar Energy and Beyond. *Coord. Chem. Rev.* **2013**, *257*, 171−186.
(9) Li, W. X. Photocatalysis of Oxide Semiconductors. *J. Aust. Ceram. Soc.* **2013**, *49*, 41−46.
(10) Asahi, R.; Morikawa, T.; Ohwaki, T.; Aoki, K.; Taga, Y. Visible-Light Photocatalysis in Nitrogen-Doped Titanium Oxides. *Science* **2001**, *293*, 269−271.
(11) Sakthivel, S.; Kisch, H. Daylight Photocatalysis by Carbon-Modified Titanium Dioxide. *Angew. Chem., Int. Ed.* **2003**, *42*, 4908−4911.
(12) Tayade, R. J.; Kulkarni, R. G.; Jasra, R. V. Transition Metal Ion Impregnated Mesoporous TiO_2 for Photocatalytic Degradation of Organic Contaminants in Water. *Ind. Eng. Chem. Res.* **2006**, *45*, 5231−5238.
(13) Jo, W. K.; Yang, C. H. Visible-light-induced Photocatalysis of Low-level Methyl-Tertiary Butyl ether (MTBE) and Trichloroethylene (TCE) using Element-doped Titanium Dioxide. *Build. Environ.* **2010**, *45*, 819−824.
(14) Natarajan, T. S.; Natarajan, K.; Bajaj, H. C.; Tayade, R. J. Enhanced Photocatalytic Activity of Bismuth-doped TiO_2 Nanotubes under Direct Sunlight Irradiation for Degradation of Rhodamine B dye. *J. Nanopart. Res.* **2013**, *15*, 1−18.
(15) Rawal, S. B.; Bera, S.; Lee, D.; Jang, D.-J.; Lee, W. I. Design of Visible-Light Photocatalysts by Coupling of Narrow Bandgap Semiconductors and TiO_2: Effect of their Relative Energy Band Positions on the Photocatalytic Efficiency. *Catal. Sci. Technol.* **2013**, *3*, 1822−1830.
(16) Hussein, A. M.; Mahoney, L.; Peng, R.; Kibombo, H.; Wu, C.-M.; Koodali, R. T.; Shende, R. Mesoporous Coupled ZnO/TiO_2 Photocatalyst Nanocomposites for Hydrogen Generation. *J. Renewable Sustainable Energy* **2013**, *5*, 033118.
(17) Vaiano, V.; Sacco, O.; Sannino, D.; Ciambelli, P. Process Intensification in the Removal of Organic Pollutants from Wastewater using Innovative Photocatalysts obtained Coupling Zinc Sulfide based Phosphors with Nitrogen Doped Semiconductors. *J. Cleaner Prod.* **2015**, *100*, 208−211.
(18) Sacco, O.; Vaiano, V.; Han, C.; Sannino, D.; Dionysiou, D. D. Photocatalytic Removal of Atrazine using N-doped TiO_2 Supported on Phosphors. *Appl. Catal., B* **2015**, *164*, 462−474.
(19) Lu, Q.; Hu, J.; Tang, K.; Qian, Y.; Zhou, G.; Liu, X. Synthesis of Nanocrystalline $CuMS_2$ (M = In or Ga) through a Solvothermal Process. *Inorg. Chem.* **2000**, *39*, 1606−1607.
(20) Banger, K. K.; Jin, M. H. C.; Harris, J. D.; Fanwick, P. E.; Hepp, A. F. A New Facile Route for the Preparation of Single-Source

DOI: 10.1021/acsami.5b03935
ACS Appl. Mater. Interfaces 2015, 7, 17138−17154

Precursors for Bulk, Thin-Film, and Nanocrystallite I–III–VI Semiconductors. *Inorg. Chem.* **2003**, *42*, 7713–7715.
(21) Castro, S. L.; Bailey, S. G.; Raffaelle, R. P.; Banger, K. K.; Hepp, A. F. Nanocrystalline Chalcopyrite Materials ($CuInS_2$ and $CuInSe_2$) via Low-Temperature Pyrolysis of Molecular Single-Source Precursors. *Chem. Mater.* **2003**, *15*, 3142–3147.
(22) Gou, X.; Cheng, F.; Shi, Y.; Zhang, L.; Peng, S.; Shen, J.; Chen, P. Shape-Controlled Synthesis of Ternary Chalcogenide $ZnIn_2S_4$ and $CuIn(S,Se)_2$ Nano-/Microstructures via Facile Solution Route. *J. Am. Chem. Soc.* **2006**, *128*, 7222–7229.
(23) Lei, Z.; You, W.; Liu, M.; Zhou, G.; Takata, T.; Hara, M.; Domen, K.; Li, C. Photocatalytic Water Reduction under Visible Light on a Novel $ZnIn_2S_4$ Catalyst Synthesized by Hydrothermal Method. *Chem. Commun.* **2003**, 2142–2143.
(24) Kale, B. B.; Baeg, J. O.; Lee, S. M.; Chang, H.; Moon, S. J.; Lee, C. W. $CdIn_2S_4$ Nanotubes and Marigold Nanostructures: A Visible-Light Photocatalyst. *Adv. Funct. Mater.* **2006**, *16*, 1349–1354.
(25) Ding, J.; Sun, S.; Yan, W.; Bao, J.; Gao, C. Photocatalytic H_2 evolution on a Novel $CaIn_2S_4$ Photocatalyst under Visible Light Irradiation. *Int. J. Hydrogen Energy* **2013**, *38*, 13153–13158.
(26) Ding, J.; Hong, B.; Luo, Z.; Sun, S.; Bao, J.; Gao, C. Mesoporous Monoclinic $CaIn_2S_4$ with Surface Nanostructure: An Efficient Photocatalyst for Hydrogen Production under Visible Light. *J. Phys. Chem. C* **2014**, *118*, 27690–27697.
(27) Shen, S.; Zhao, L.; Zhou, Z.; Guo, L. Enhanced Photocatalytic Hydrogen Evolution over Cu-doped $ZnIn_2S_4$ under Visible Light Irradiation. *J. Phys. Chem. C* **2008**, *112*, 16148–16155.
(28) Hou, J.; Yang, C.; Cheng, H.; Wang, Z.; Jiao, S.; Zhu, H. Ternary 3D Architectures of CdS QDs/Graphene/$ZnIn_2S_4$ Heterostructures for Efficient Photocatalytic H_2 Production. *Phys. Chem. Chem. Phys.* **2013**, *15*, 15660–15668.
(29) Yu, Y.; Chen, G.; Wang, G.; Lv, Z. Visible-light-driven $ZnIn_2S_4$/$CdIn_2S_4$ Composite Photocatalyst with Enhanced Performance for Photocatalytic H_2 Evolution. *Int. J. Hydrogen Energy* **2013**, *38*, 1278–1285.
(30) Ding, J.; Yan, W.; Sun, S.; Bao, J.; Gao, C. Hydrothermal Synthesis of $CaIn_2S_4$-Reduced Graphene Oxide Nanocomposites with Increased Photocatalytic Performance. *ACS Appl. Mater. Interfaces* **2014**, *6*, 12877–12884.
(31) Yang, S.; Li, L.; Yuan, W.; Xia, Z. Enhanced Visible Light Photocatalytic Activity of $ZnIn_2S_4$ modified by Semiconductors. *Dalton Trans.* **2015**, *44*, 6374–6383.
(32) Boxi, S. S.; Paria, S. Effect of Silver Doping on TiO_2, CdS, and ZnS Nanoparticles for the Photocatalytic Degradation of Metronidazole under Visible Light. *RSC Adv.* **2014**, *4*, 37752–37760.
(33) Liu, J.; Zhang, G.; Yu, J. C.; Guo, Y. In situ Synthesis of Zn_2GeO_4 Hollow Spheres and their Enhanced Photocatalytic Activity for the Degradation of Antibiotic Metronidazole. *Dalton Trans.* **2013**, *42*, 5092–5099.
(34) Dong, S.; Sun, J.; Li, Y.; Yu, C.; Li, Y.; Sun, J. $ZnSnO_3$ Hollow Nanospheres/Reduced Graphene Oxide Nanocomposites as High-performance Photocatalysts for Degradation of Metronidazole. *Appl. Catal., B* **2014**, *144*, 386–393.
(35) Dong, S.; Li, Y.; Sun, J.; Yu, C.; Li, Y.; Sun, J. Facile Synthesis of Novel ZnO/RGO Hybrid Nanocomposites with Enhanced Catalytic Performance for Visible-Light-Driven Photodegradation of Metronidazole. *Mater. Chem. Phys.* **2014**, *145*, 357–365.
(36) Yu, C.; Dong, S.; Feng, J.; Sun, J.; Hu, L.; Li, Y.; Sun, J. Controlled Synthesis of Uniform $BiVO_4$ Microcolumns and Advanced Visible-Light-Driven Photocatalytic Activity for the Degradation of Metronidazole-contained Wastewater. *Environ. Sci. Pollut. Res.* **2014**, *21*, 2837–2845.
(37) Li, J.; Zhao, W.; Guo, Y.; Wei, Z.; Han, M.; He, H.; Yang, S.; Sun, C. Facile Synthesis and High Activity of Novel $BiVO_4$/$FeVO_4$ Heterojunction Photocatalyst for Degradation of Metronidazole. *Appl. Surf. Sci.* **2015**, *351*, 270–279.
(38) Xu, Y.; Zhang, W.-D. CdS/g-C_3N_4 Hybrids with Improved Photostability and Visible Light Photocatalytic Activity. *Eur. J. Inorg. Chem.* **2015**, *2015*, 1744–1751.
(39) Almaraz, E. G.; Reyes, L. H.; Quintero, A. C.; Ruiz, E. R.; Ramirez, A. H.; Guzman-Mar, J. L. Potential of Multisyringe Chromatography for the On-line Monitoring of the Photocatalytic Degradation of Antituberculosis Drugs in Aqueous Solution. *Chemosphere* **2015**, *121*, 68–75.
(40) Natarajan, T. S.; Bajaj, H. C.; Tayade, R. J. Enhanced Direct Sunlight Photocatalytic Oxidation of Methanol using Nanocrystalline TiO_2 Calcined at Different Temperature. *J. Nanopart. Res.* **2014**, *16* (2713), 1–16.
(41) Shen, S.; Zhao, L.; Guo, L. Cetyltrimethylammoniumbromide (CTAB)-Assisted Hydrothermal Synthesis of $ZnIn_2S_4$ as an Efficient Visible-Light-Driven Photocatalyst for Hydrogen Production. *Int. J. Hydrogen Energy* **2008**, *33*, 4501–4510.
(42) Chen, Y.; Hu, S.; Liu, W.; Chen, X.; Wu, L.; Wang, X.; Liu, P.; Li, Z. Controlled Syntheses of Cubic and Hexagonal $ZnIn_2S_4$ Nanostructures with Different Visible-light Photocatalytic Performance. *Dalton Trans.* **2011**, *40*, 2607–2613.
(43) Liu, B.; Zeng, H. C. Mesoscale Organization of CuO Nanoribbons: Formation of Dandelions. *J. Am. Chem. Soc.* **2004**, *126*, 8124–8125.
(44) Liu, B.; Zeng, H. C. Fabrication of ZnO Dandelions via a Modified Kirkendall Process. *J. Am. Chem. Soc.* **2004**, *126*, 16744–16746.
(45) Chaudhari, N. S.; Bhirud, A. P.; Sonawane, R. S.; Nikam, L. K.; Warule, S. S.; Rane, V. H.; Kale, B. B. Ecofriendly Hydrogen Production from Abundant Hydrogen Sulfide using Solar light-Driven Hierarchical Nanostructured $ZnIn_2S_4$ Photocatalyst. *Green Chem.* **2011**, *13*, 2500–2506.
(46) Erdem, B.; Hunsicker, R. A.; Simmons, G. W.; Sudol, E. D.; Dimonie, V. L.; El-Aasser, M. S. XPS and FTIR Surface Characterization of TiO_2 Particles Used in Polymer Encapsulation. *Langmuir* **2001**, *17*, 2664–2669.
(47) Zhong, Q.; Vohs, J. M.; Bonnell, D. A. Effect of Reduction on the Topographic and Electronic Structure of TiO_2 (110) Surfaces. *Surf. Sci.* **1992**, *274*, 35–43.
(48) Shi, J.; Chen, J.; Feng, Z.; Chen, T.; Lian, Y.; Wang, X.; Li, C. Photoluminescence Characteristics of TiO_2 and Their Relationship to the Photoassisted Reaction of Water/Methanol Mixture. *J. Phys. Chem. C* **2007**, *111*, 693–699.
(49) Zhao, Y.; Li, C.; Liu, X.; Gu, F.; Jiang, H.; Shao, W.; Zhang, L.; He, Y. Synthesis and Optical Properties of TiO_2 Nanoparticles. *Mater. Lett.* **2007**, *61*, 79–83.
(50) Zhang, H.; Xie, C.; Zhang, Y.; Liu, G.; Li, Z.; Liu, C.; Ma, X.; Zhang, W. F. Effects of Thermal Treatment under Different Atmospheres on the Spectroscopic Properties of Nanocrystalline TiO_2. *J. Appl. Phys.* **2008**, *103*, 103107.
(51) Xiong, L. B.; Li, J. L.; Yang, B.; Yu, Y. Ti^{3+} in the Surface of Titanium Dioxide: Generation, Properties and Photocatalytic Application. *J. Nanomater.* **2011**, *2012*, 831524.10.1155/2012/831524
(52) Mathew, S.; Prasad, A. K.; Benoy, T.; Rakesh, P. P.; Hari, M.; Libish, T. M.; Radhakrishnan, P.; Nampoori, V. P. N.; Vallabhan, C. P. G. UV-Visible Photoluminescence of TiO_2 Nanoparticles Prepared by Hydrothermal Method. *J. Fluoresc.* **2012**, *22*, 1563–1569.
(53) Santara, B.; Giri, P. K.; Imakita, K.; Fujii, M. Evidence of Oxygen Vacancy Induced Room Temperature Ferromagnetism in Solvothermally Synthesized Undoped TiO_2 Nanoribbons. *Nanoscale* **2013**, *5*, 5476–5488.
(54) Santara, B.; Giri, P. K.; Imakita, K.; Fujii, M. Evidence for Ti Interstitial Induced Extended Visible Absorption and Near Infrared Photoluminescence from Undoped TiO_2 Nanoribbons: An In Situ Photoluminescence Study. *J. Phys. Chem. C* **2013**, *117*, 23402–23411.
(55) Yu, J.; Wang, S.; Low, J.; Xiao, W. Enhanced photocatalytic performance of direct Z-scheme g-C_3N_4–TiO_2 photocatalysts for the decomposition of formaldehyde in air. *Phys. Chem. Chem. Phys.* **2013**, *15*, 16883–16890.
(56) Shifu, C.; Lei, J.; Wenming, T.; Xianliang, F. Fabrication, Characterization and Mechanism of a Novel Z-scheme Photocatalyst $NaNbO_3$/WO_3 with Enhanced Photocatalytic Activity. *Dalton Trans.* **2013**, *42*, 10759–10768.

DOI: 10.1021/acsami.5b03935
ACS Appl. Mater. Interfaces 2015, 7, 17138–17154

(57) Katsumata, H.; Tachi, Y.; Suzuki, T.; Kaneco, S. Z-scheme Photocatalytic Hydrogen Production over WO_3/g-C_3N_4 Composite Photocatalysts. *RSC Adv.* **2014**, *4*, 21405−21409.
(58) Bai, Y.; Wang, P. Q.; Liu, J. Y.; Liu, X.-J. Enhanced Photocatalytic Performance of Direct Z-scheme BiOCl-g-C_3N_4 Photocatalysts. *RSC Adv.* **2014**, *4*, 19456−19461.
(59) Zhang, J.; Hu, Y.; Jiang, X.; Chen, S.; Meng, S.; Fu, X. Design of a Direct Z-scheme Photocatalyst: Preparation and Characterization of Bi_2O_3/g-C_3N_4 with High Visible Light Activity. *J. Hazard. Mater.* **2014**, *280*, 713−722.
(60) Chen, S.; Hu, Y.; Ji, L.; Jiang, X.; Fu, X. Preparation and Characterization of Direct Z-scheme Photocatalyst Bi_2O_3/$NaNbO_3$ and Its Reaction Mechanism. *Appl. Surf. Sci.* **2014**, *292*, 357−366.
(61) Tian, N.; Huang, H.; He, Y.; Guo, Y.; Zhang, T.; Zhang, Y. Mediator-Free Direct Z-scheme Photocatalytic System: $BiVO_4$/g-C_3N_4 Organic-Inorganic Hybrid Photocatalyst With Highly Efficient Visible-Light Induced Photocatalytic Activity. *Dalton Trans.* **2015**, *44*, 4297−4307.
(62) Meng, S.; Ning, X.; Zhang, T.; Chen, S. F.; Fu, X. What is the Transfer Mechanism of Photogenerated Carriers for the Nanocomposite Photocatalyst Ag_3PO_4/g-C_3N_4, Band-Band Transfer or a Direct Z-scheme? *Phys. Chem. Chem. Phys.* **2015**, *17*, 11577−11585.
(63) He, Y.; Zhang, L.; Fan, M.; Wang, X.; Walbridge, M. L.; Nong, Q.; Wu, Y.; Zhao, L. Z-scheme SnO_{2-x}/g-C_3N_4 Composite as an Efficient Photocatalyst for Dye Degradation and Photocatalytic CO_2 Reduction. *Sol. Energy Mater. Sol. Cells* **2015**, *137*, 175−184.
(64) Wang, J.-C.; Zhang, L.; Fang, W.-X.; Ren, J.; Li, Y.-Y.; Yao, H.-C.; Wang, J.-S.; Li, Z.-J. Enhanced Photoreduction CO_2 Activity over Direct Z-Scheme α-Fe_2O_3/Cu_2O Heterostructures under Visible Light Irradiation. *ACS Appl. Mater. Interfaces* **2015**, *7*, 8631−8639.
(65) Kumar, S.; Baruah, A.; Tonda, S.; Kumar, B.; Shanker, V.; Sreedhar, B. Cost-Effective and Eco-Friendly Synthesis of Novel and Stable N-doped ZnO/g-C_3N_4 Core−Shell Nanoplates with Excellent Visible-Light Responsive Photocatalysis. *Nanoscale* **2014**, *6*, 4830−4842.

DOI: 10.1021/acsami.5b03935
ACS Appl. Mater. Interfaces 2015, 7, 17138−17154